nature microbiology

Article

https://doi.org/10.1038/s41564-026-02269-8

Gut microbial ammonia enhances colonic acetylcholine levels to regulate intestinal motility

Received: 20 July 2025

Accepted: 19 January 2026

Published online: 20 February 2026

Check for updates

Hao Chen[1,3], Zhen Wang[1,3], Yiming Zhao[1], Wenyu Yang[2], Jing Huang[2] & Zheng Yu[1]

Intestinal motility is a function of the enteric nervous system involving secretion of the excitatory neurotransmitter acetylcholine (ACh). Although gut commensal bacteria are key regulators of intestinal physiology, the molecular mechanisms underlying microbial influence on intestinal peristalsis and constipation remain unclear. Here we report a link between microbial nitrogen metabolism and intestinal motility regulation via ammonia production. We observed compensatory elevation of intestinal ammonia levels and urease activity in mouse models of intestinal dysmotility, induced by ACh deficiency, and in patients with constipation. Ammonia supplementation or intervention in mice with the urease-positive *Lysinibacillus fusiformis* isolated from patient stool, or engineered urease-expressing bacteria, effectively restored colonic ACh levels. In vitro, ammonia upregulated the expression of voltage-gated calcium channels on enteric neurons, driving Ca^{2+} influx to potentiate ACh secretion. Our study reveals a microbial compensatory mechanism that responds to fluctuating ACh levels in the intestine and provides microbial targets for intestinal motility disorders.

Intestinal peristalsis is an enteric nervous system (ENS)-regulated reflex[1]. Acetylcholine (ACh) functions as a pivotal excitatory neurotransmitter in this process[2]. Dysregulation of ACh signalling is closely linked to various intestinal motility disorders. Clinical evidence demonstrates significantly reduced ACh release in colonic tissues of patients with chronic constipation[3]. Exogenous ACh supplementation effectively enhances intestinal motility[4]. Consequently, ACh occupies a central role in maintaining physiological intestinal peristalsis[5]. Beyond intrinsic ENS regulation, microbial dysbiosis is widely recognized as an important driver of gastrointestinal pathologies[6]. Studies demonstrated that microbiota depletion disrupted neurogenic motor programmes and prolonged intestinal transit time[7,8]. Crucially, microbiota reconstitution in adult germ-free mice restores enteric neuronal excitability, providing robust evidence for the microbiota's essential role in regulating intestinal neural activity and motility[9]. However, the detailed molecular mechanisms underlying direct and specific microbial regulation of ENS neuronal activity and peristaltic outcomes remain an unresolved scientific question in the field.

Ammonia is primarily generated in the gut through microbial urease-mediated nitrogen metabolism and has long been regarded as a metabolic waste product[10]. However, recent studies demonstrate that gut-derived ammonia can modulate host social anxiety and enhance enteric neuromuscular transmission, suggesting a previously underappreciated signalling role[11,12]. Here, our study reveals that ACh deficiency triggers adaptive responses in the gut microbiota, leading to compensatory ammonia production. Endogenous ammonia modulates the expression of voltage-gated calcium channel Cav2.1 on enteric neuronal presynaptic terminals. This modulation

[1]Human Microbiome and Health Group, Department of Microbiology, Xiangya School of Basic Medical Sciences, Central South University, Changsha, China. [2]Human Microbiome and Health Group, Department of Parasitology, Xiangya School of Basic Medical Sciences, Central South University, Changsha, China. [3]These authors contributed equally: Hao Chen, Zhen Wang. e-mail: yuzheng@csu.edu.cn

enhances Ca^{2+} influx, thereby effectively promoting ACh release and restoring normal propulsive peristalsis. This discovery uncovers a microbiota–host interaction mechanism: the gut microbiota responds to intestinal physiological perturbations and produces metabolites to provide compensatory feedback, dynamically maintaining intestinal physiological homeostasis.

Reduced ACh triggers compensatory ammonia production by gut microbiota

To elucidate intestinal motility responses to ACh deficiency, mice were administered loperamide (LOP) via oral gavage (Fig. 1a). Colonic ACh levels were significantly reduced in LOP-treated mice (Fig. 1b). Concurrently, whole intestinal transit (WIT) time markedly increased, Bristol stool scores and faecal water content decreased, small intestinal transit (SIT) rate diminished, and bead expulsion time was delayed, collectively indicating impaired intestinal motility (Fig. 1c). Exogenous ACh supplementation significantly decreased WIT time in LOP-treated mice, confirming the essential role of ACh in maintaining intestinal motility (Fig. 1d).

LOP-induced dysmotility was accompanied by substantial reductions in colonic ACh levels. To evaluate the impact of dysmotility on the gut microbiome, metagenomic sequencing was performed. Non-metric multidimensional scaling (NMDS) analysis based on Bray–Curtis distances revealed that LOP significantly altered the composition of functional genes in the gut microbiome (Fig. 1e). Notably, microbial genes involved in acetylcholine and choline metabolism showed no significant changes in abundance in either LOP-treated mice or patients with constipation, suggesting that microbial response to ACh deficiency does not involve direct modulation of ACh metabolism (Extended Data Fig. 1). Then, differential abundance analysis identified ko00230 (purine metabolism) as the most enriched Kyoto Encyclopedia of Genes and Genomes (KEGG) pathway within the 'microbial metabolism' category (Fig. 1f and Extended Data Fig. 2a). Within this pathway, *ureA* (k01430) exhibited the greatest fold change among all differential genes (Fig. 1g). As *ureA* encodes a structural subunit of urease (EC 3.5.1.5), which catalyses urea hydrolysis to ammonia, this increase suggests a potential role for bacterial urease in intestinal dysmotility. Consistently, most urea catabolism-related pathways and urease gene clusters (*ure* operon family) were significantly upregulated following LOP treatment (Fig. 1h–j). Furthermore, public gut metagenomes from patients with constipation cohorts also demonstrated elevated urease abundance, indicating that this response is associated with intestinal motility disorders. (Extended Data Fig. 2b,c). As urease is the only enzyme responsible for microbial urea-to-ammonia conversion, faecal ammonia concentration and colonic urease activity were measured, and found to be significantly elevated after motility impairment, which was also reproduced in patients with constipation (Fig. 1k and Supplementary Table 1). Moreover, in vitro faecal culture experiments showed that LOP did not directly alter microbial community composition or urease activity, indicating that enrichment of urease-positive bacteria is secondary to dysmotility rather than a direct effect of LOP (Extended Data Fig. 3). Since mammals lack endogenous urea-metabolizing enzymes, these findings indicate enhanced microbial urea metabolism during dysmotility.

To determine temporal relationships between ACh decline and ammonia elevation, both parameters were measured daily for 4 days following LOP intervention (Fig. 1l). Colonic ACh significantly decreased within 24 h, whereas faecal ammonia increased significantly at 48 h, indicating that ACh reduction precedes ammonia elevation (Fig. 1l). Cross-correlation function (CCF) analysis revealed a significant negative correlation only when ammonia changes lagged behind ACh by 24 h, suggesting that increased ammonia production represents a compensatory microbial response to ACh deficiency-induced dysmotility (Fig. 1m). As ammonia neutralizes protons and contributes to bacterial acid-resistance mechanisms, colonic pH was monitored after LOP treatment[13,14] (Extended Data Fig. 4a). Colonic pH significantly decreased within 24–48 h and subsequently rebounded, suggesting that transient acidification triggers compensatory microbial ammonia production (Extended Data Fig. 4b).

To investigate the functional role of microbially derived ammonia, LOP-treated mice were administrated with flurofamide (FFA), a potent and specific bacterial urease inhibitor (Fig. 1n). FFA markedly reduced faecal ammonia, confirming effective inhibition of microbial ammonia production (Fig. 1o). Ammonia levels positively correlated with changes in colonic ACh, and urease inhibition significantly exacerbated intestinal dysmotility (Fig. 1p,q). In contrast, FFA increased urea levels, which were negatively correlated with colonic ACh changes, indicating that ammonia, rather than urea, is the relevant regulatory metabolite (Extended Data Fig. 5a–f). Collectively, these results demonstrate that ACh deficiency induces compensatory microbial ammonia production to maintain intestinal motility homeostasis.

The urease-positive isolate *Lysinibacillus fusiformis* elevates colonic ACh levels via ammonia production

Given the importance of urease-positive bacteria, we examined taxonomic shifts post LOP intervention using intestinal metagenomic data. LOP-induced constipation was accompanied by reduced colonic ACh levels, altered microbial composition and impaired intestinal motility (Extended Data Fig. 2d,e). We annotated bacteria harbouring the *ure* operon and ranked their contributions at the order level. Bacteroidales, Rhizobiales and Bacillales contributed the most, all showing significant increases following dysmotility (Fig. 2a). To identify key urease-positive strains, urease-producing bacteria were isolated from stool samples of constipated volunteers using phenol red urea medium (Fig. 2b). A total of 19 urease-positive isolates were obtained, predominantly belonging to Bacillales and Lactobacillales (Fig. 2b and Supplementary Table 2). Metagenomic analysis of both LOP-treated mice and constipation cohorts revealed that only *Lysinibacillus fusiformis* increased significantly during dysmotility and positively correlated with faecal and blood ammonia levels (Fig. 2c,d and Extended Data Fig. 6a,b). Although urease gene (*ureC*) expression increased in multiple strains, only *L. fusiformis* exhibited a significant increase in copy number (Extended Data Fig. 6c). Moreover, *L. fusiformis* displayed enhanced urease activity under acidic conditions (pH 5), supporting its role as a key responder to dysmotility-associated luminal acidification (Extended Data Fig. 4c). To functionally validate its role, *L. fusiformis* was administered to antibiotic-pretreated, LOP-treated mice (Fig. 2e). Supplementation significantly elevated faecal ammonia and colonic ACh levels and improved intestinal motility (Fig. 2e and Extended Data Fig. 7a). These effects were abolished upon co-treatment with the urease inhibitor FFA, which reduced ACh levels and further impaired motility (Fig. 2f and Extended Data Fig. 7b,c). Histological assessment showed that LOP-induced dysmotility caused crypt distortion, goblet cell vacuolation and inflammatory infiltration, all of which were alleviated by *L. fusiformis* supplementation (Fig. 2g and Extended Data Fig. 7d).

To further establish the role of urease, *Escherichia coli* BL21 was engineered to heterologously express *ureABC* from *L. fusiformis*. Whole-genome sequencing confirmed that *ureABC* is present as a single-copy operon in *L. fusiformis* (Extended Data Fig. 7e). The three structural subunits were cloned into two compatible ColE1-origin plasmids. PCR screening of ten randomly selected colonies verified the simultaneous presence of all three genes, and qPCR demonstrated comparable plasmid copy numbers, indicating stable plasmid coexistence without mutual exclusion (Extended Data Fig. 8a,b). Serial passaging experiments demonstrated that over 80% of colonies retained both plasmids after 40 generations without antibiotic selection (Extended Data Fig. 8c–e). Although recombinant urease activity was lower than that of native *L. fusiformis*, Ni^{2+} supplementation markedly enhanced enzymatic activity (Extended Data Fig. 8f). Tris-tricine

https://doi.org/10.1038/s41564-026-02269-8

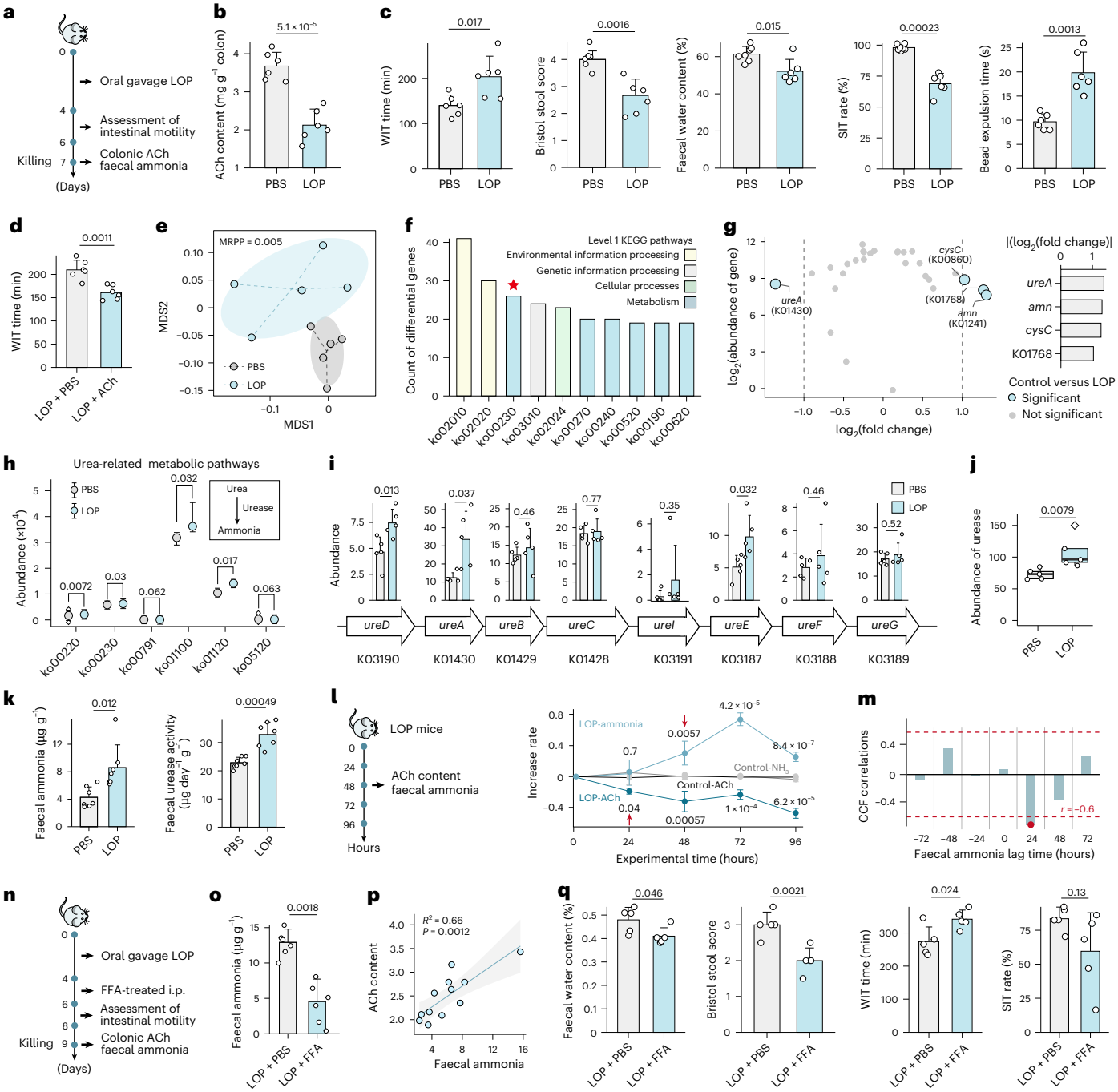


Fig. 1 | Reduced ACh triggers compensatory ammonia production by gut microbiota. a, Experimental design for inducing ACh deficiency using LOP. In brief, mice ($n = 6$ per group) were administered LOP via oral gavage from days 0–4. Intestinal motility was assessed from days 4–6. On day 7, the mice were euthanized for the measurement of colonic ACh and faecal ammonia levels. **b**, Change in colonic ACh levels after LOP treatment ($n = 6$ per group). **c**, Assessment of intestinal motility on LOP mice including WIT time, Bristol stool score, faecal water content, SIT time and bead expulsion time ($n = 6$ per group). **d**, Alterations in WIT time following exogenous ACh oral administration in LOP mice ($n = 6$ per group). **e**, NMDS analysis based on Bray–Curtis distance of gut microbiome functional gene (based on KEGG annotation) from control ($n = 5$) and LOP-treated ($n = 5$) mice. Each point represents the functional gene composition of a single faecal metagenomic sample. **f**, KEGG pathway enrichment of differentially abundant functional genes. **g**, Differential abundance of genes within KEGG pathway ko00230. Right: ranked $\log_2$ fold-change values. **h**, Changes in abundance of urea metabolism-related pathways ($n = 5$ per group). **i**, Change in relative abundance of *ure* operons (annotated by KEGG Orthology identifiers) after LOP treatment ($n = 5$ per group). **j**, Change in abundance of predicted urease after LOP treatment ($n = 5$ per group). **k**, Faecal ammonia levels and urease enzymatic activity in LOP-treated mice ($n = 7$ per group). **l**, Longitudinal sampling schematic (left) and temporal dynamics of colonic ACh and faecal ammonia concentrations (right) ($n = 6$ per group). Red arrow indicates onset of significant divergence in trajectories between groups. **m**, CCF analysis between colonic ACh and faecal ammonia levels. Red point indicates time-lagged correlation peak achieving statistical significance. **n**, Experimental design for FFA treatment of LOP-treated mice ($n = 6$ per group). **o**, Modulation of faecal ammonia levels by FFA treatment of LOP-treated mice ($n = 6$ per group). **p**, Regression analysis of colonic ACh levels and faecal ammonia levels. Solid lines represent ordinary least-squares linear regressions, and error bands indicate 95% confidence intervals. **q**, Assessment of intestinal motility of FFA-treated LOP mice ($n = 5$ per group). Data represent mean ± s.d. of at least 3 biologically independent experiments, except for boxplots in **j** (centre line or point, median; box limits, 25th and 75th percentiles; whiskers, Tukey's method (1.5× interquartile range); diamond, outliers). Statistical significance was assessed using two-tailed Student's *t*-test. MRPP, multi-response permutation procedure. Illustrations in **a**, **l** and **n** created in BioRender; Chen, H. https://biorender.com/foe3u8n (2026).

https://doi.org/10.1038/s41564-026-02269-8

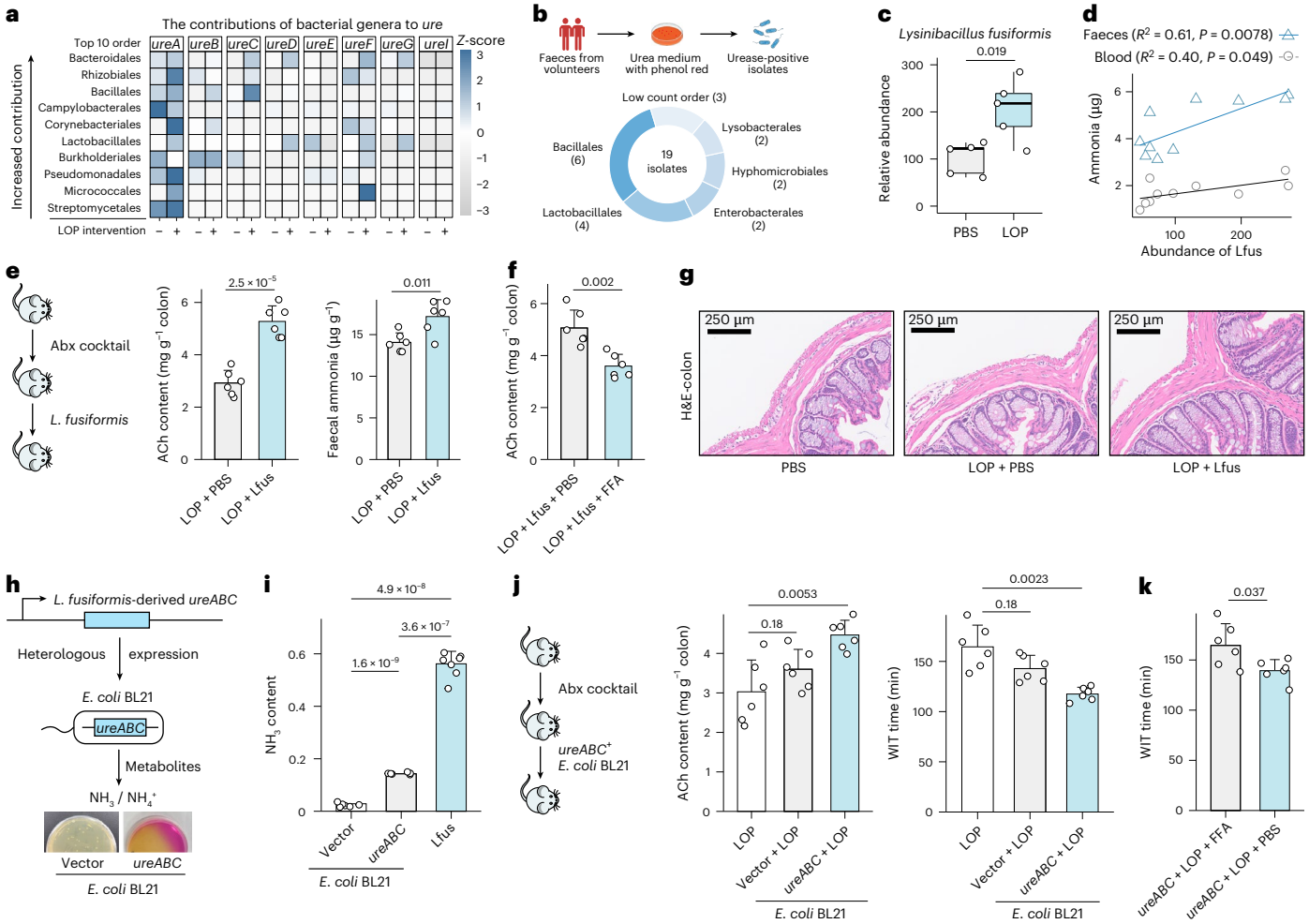


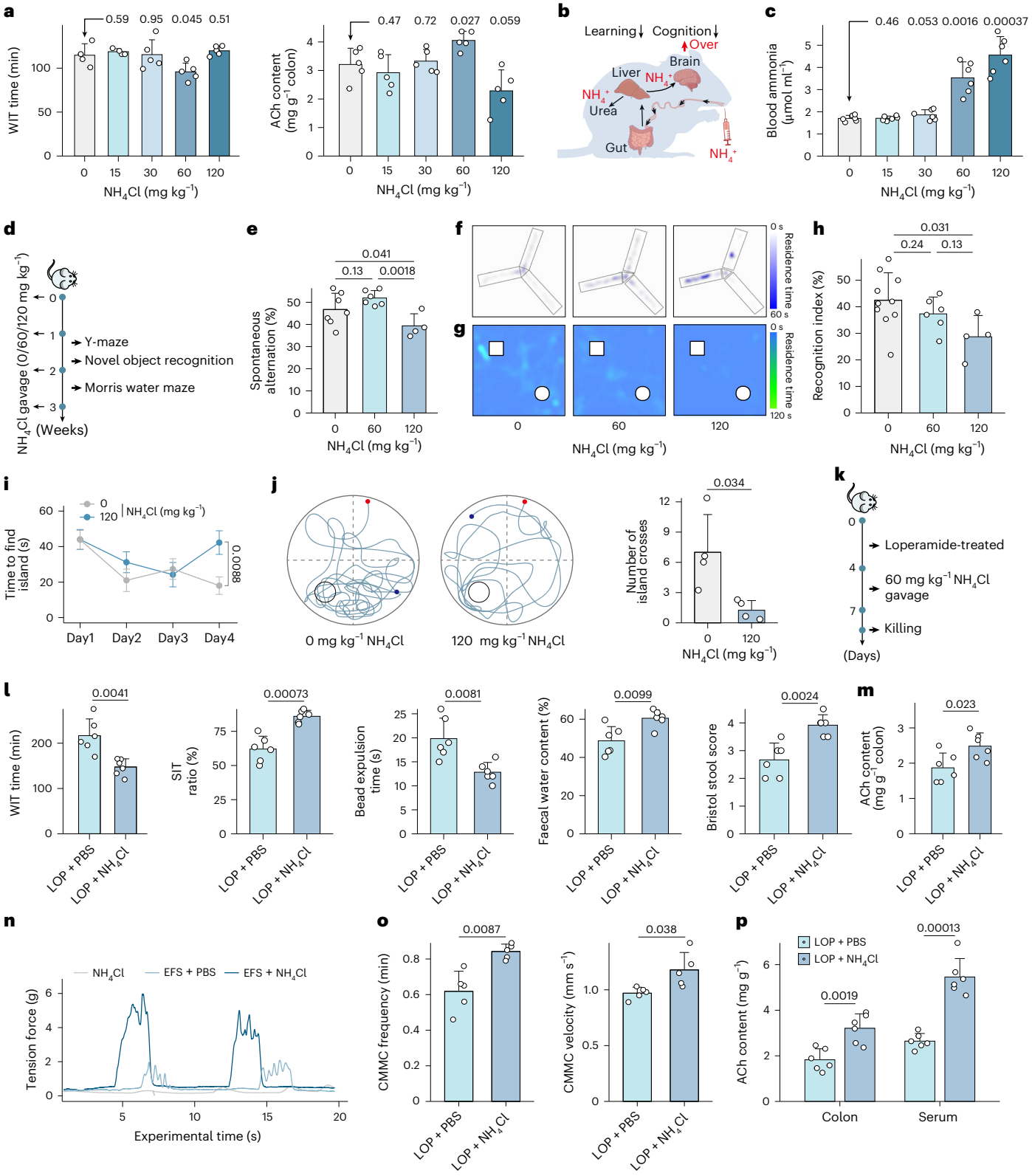
Fig. 2 | Urease-positive isolate *L. fusiformis* increases colonic ACh levels via ammonia production. a, Contribution of the top 10 bacterial orders to the *ure* operons. **b**, Screening strategy and taxonomic classification (order-level) of urease-positive isolates from constipated stool. **c**, Differential abundance of *L. fusiformis* between the two indicated groups ($n = 5$ per group). **d**, Regression analysis correlating *L. fusiformis* (Lfus) abundance with faecal and blood ammonia concentrations. Solid lines represent ordinary least-squares linear regressions. **e**, Alterations in colonic ACh and faecal ammonia concentrations in LOP-treated mice ($n = 6$ per group) administered with *L. fusiformis*. **f**, Modulation of colonic ACh concentrations by FFA treatment in LOP-treated mice ($n = 6$ per group) administered with *L. fusiformis*. **g**, Representative hematoxylin and eosin (H&E)-stained sections of colonic tissue in LOP-treated mice administered with or without *L. fusiformis*. **h**, Experimental workflow for heterologous expression of *L. fusiformis*-derived *ureABC* in *E. coli* BL21. **i**, Urease enzymatic activity of recombinant BL21. *E. coli* BL21 and *L. fusiformis* served as controls ($n = 6$ per group). **j**, Changes in colonic ACh and WIT time in LOP-treated mice ($n = 6$ per group) administered with or without recombinant *E. coli* BL21. **k**, Modulation of WIT time by FFA treatment in LOP-treated mice ($n = 6$ per group) administered with recombinant *E. coli* BL21. Data represent mean ± s.d. of at least 3 biologically independent experiments, except for boxplots in **c** (centre line or point, median; box limits, 25th and 75th percentiles; whiskers, Tukey's method (1.5× interquartile range)). Statistical significance was assessed using two-tailed Student's *t*-test. Illustrations in **b**, **e** and **j** created in BioRender; Chen, H. https://biorender.com/foe3u8n (2026).

sodium dodecyl sulfate–polyacrylamide gel electrophoresis (SDS–PAGE) and liquid chromatography–mass spectrometry (LC–MS) confirmed expression of all three urease subunits (Extended Data Fig. 8g). Importantly, IPTG-induced recombinant BL21 retained urease activity after oral administration and significantly increased faecal urease and ammonia levels in vivo (Fig. 2j and Extended Data Fig. 8h). Quantitative (q)PCR analysis confirmed successful colonic colonization with stable plasmid maintenance (Extended Data Fig. 8i,j). In LOP-treated mice, recombinant BL21 elevated colonic ACh levels and accelerated intestinal transit, whereas FFA abolished these effects (Fig. 2j,k). Together, these results demonstrate that *L. fusiformis* enhances intestinal ACh via urease-dependent ammonia production.

Physiological concentration of NH_4Cl elevates colonic ACh levels without inducing toxicity

To determine whether ammonia is the key effector driving increased colonic ACh levels, we performed exogenous NH_4Cl supplementation and assessed its direct impact. Dose–response analysis (0, 15, 30, 60 and 120 mg kg^{-1}) showed that only the 60 mg kg^{-1} NH_4Cl significantly shortened WIT time and increased colonic ACh levels (Fig. 3a). Systemically absorbed ammonia is primarily detoxified to urea in the liver, whereas excessive ammonia may cross the blood–brain barrier and impair cognition (Fig. 3b). To evaluate the safety of different NH_4Cl doses, we measured blood ammonia concentrations after treatment. Both 60 and 120 mg kg^{-1} NH_4Cl significantly increased blood ammonia levels, suggesting a potential risk of toxicity (Fig. 3c). To assess whether these doses caused cognitive impairment, we assessed learning and cognitive abilities using the new object recognition test, Y-maze, and Morris water maze tests (Fig. 3d). Mice treated with 120 mg kg^{-1} NH_4Cl displayed significantly reduced spontaneous alternation (Y-maze) and decreased novel object preference, indicating impaired spatial working memory and object recognition memory (Fig. 3e–h). In contrast, the 60 mg kg^{-1} group showed no significant difference from controls (Fig. 3e–h). During the Morris water maze training phase, mice receiving

https://doi.org/10.1038/s41564-026-02269-8



120 mg kg^{-1} NH_4Cl required more time to locate the hidden platform (Fig. 3i). In the probe trial, they spent less time in the target quadrant and exhibited fewer platform crossings, confirming spatial learning and memory deficits (Fig. 3j). No impairments were observed in the 60 mg kg^{-1} group. These findings identified 60 mg kg^{-1} as an effective dose that does not induce measurable cognitive toxicity.

Subsequently, we administered NH_4Cl (60 mg kg^{-1}) by oral gavage to LOP-treated mice (Fig. 3k). To comprehensively characterize the ammonia-induced improvement, we applied a multilevel assessment integrating in vivo, ex vivo and biochemical measurement (Extended Data Fig. 9a). At the whole-animal level, ammonia supplementation markedly shortened WIT time, increased SIT rate, enhanced faecal water content, promoted colorectal propulsion and increased colonic ACh levels, collectively indicating accelerated luminal transport across the gastrointestinal tract in vivo (Fig. 3l,m). Ex vivo organ bath recordings further validated these findings. Considering that

Fig. 3 | Physiological concentration of NH_4Cl elevates colonic ACh levels without inducing toxicity. **a**, WIT time and colonic ACh concentration in mice ($n = 5$ per group) treated with different concentrations of NH_4Cl. **b**, Proposed model depicting the relationship between NH_4Cl intervention and its impact on cognitive learning deficits in mice. **c**, Blood ammonia levels in mice treated with different concentrations of NH_4Cl ($n = 6$ per group). **d**, Experimental design for assessing cognitive function and memory in mice receiving different NH_4Cl doses. **e**, Spontaneous alternation ratio in the Y-maze test ($n = 7$ in 0, $n = 6$ in 60, $n = 4$ in 120 mg kg^{-1} NH_4Cl). **f**, Residence time in the test area during testing. **g**, Heat map depicting the spatial distribution of residence time in the test area. Squares indicate novel objects, and circles indicate the retained familiar object. **h**, Changes in cognitive index derived from the novel object recognition test ($n = 7$ in 0, $n = 6$ in 60, $n = 4$ in 120). **i**, Latency to locate the hidden island during acquisition training in the Morris water maze test ($n = 4$ per group). **j**, Number of island location crosses (right) and representative swim paths (left) during the probe trial (60 s) after island removal ($n = 4$ per group). The red dots represent the starting position, and the blue dots represent the ending position. **k**, Experimental design for LOP-treated mice ($n = 6$ per group) administered with 60 mg kg^{-1} NH_4Cl. **l**, Assessment of intestinal motility in LOP-treated mice administered with NH_4Cl, including WIT time, Bristol stool score, faecal water content, SIT time and bead expulsion time ($n = 6$ per group). **m**, Change in colonic ACh content in LOP-treated mice administered with NH_4Cl ($n = 6$ per group). **n**, Representative traces of colonic muscle tension recorded in organ baths under indicated treatments. **o**, Change in CMMC frequency and CMMC velocity after NH_4Cl treatment ($n = 5$ per group). **p**, Change in ACh levels in colon and serum after in situ vascular cannulation ($n = 6$ per group). Data represent mean ± s.d. of at least three biologically independent experiments. Statistical significance was assessed using two-tailed Student's *t*-test. Illustrations in **b**, **d** and **k** created in BioRender; Chen, H. https://biorender.com/foe3u8n (2026).

the colon is the major site of microbial ammonia production and the first region exposed to locally generated ammonia, we selected colonic segments for the ex vivo experiments. Ammonia treatment significantly enhanced the contractile amplitude of colonic muscle strips and increased both the frequency and propagation velocity of colonic migrating motor complexes (CMMCs) on spatiotemporal maps, demonstrating strengthened peristaltic coordination under near-physiological conditions (Fig. 3n,o and Extended Data Fig. 9b). Furthermore, in situ vascular cannulation experiments revealed that ammonia administration elevated ACh concentrations in both colonic tissues and venous effluents, indicating increased neurotransmitter release accompanying enhanced motility (Fig. 3p). These complementary results establish that physiologically relevant concentrations of ammonia augment gut motility through coordinated enhancement of neuromuscular and secretory functions along the intestinal tract, and that ammonia is a key mediator through which urease-positive bacteria increase colonic ACh, effectively and safely at physiologically relevant concentrations without inducing cognitive toxicity.

Since ammonia is also a precursor for glutamine synthesis, we next evaluated whether glutamine metabolism contributes to the observed effects. KEGG-based metagenomic and transcriptomic analyses of both mouse and human samples revealed minimal alterations in genes involved in glutamine synthesis or degradation (Extended Data Fig. 8g). Moreover, glutamine levels increased mainly in serum, rather than in the colon, suggesting enhanced hepatic detoxification rather than local glutamine-mediated regulation (Extended Data Fig. 8h,i). Exogenous glutamine administration slightly improved colonic motility but did not elevate colonic ACh content (Extended Data Fig. 8j–l). These results indicate that glutamine metabolism does not directly contribute to the microbiota-derived ammonia–ACh regulatory pathway (Extended Data Fig. 8m).

NH_4Cl enhances ACh levels by upregulating Cav2.1 channel expression

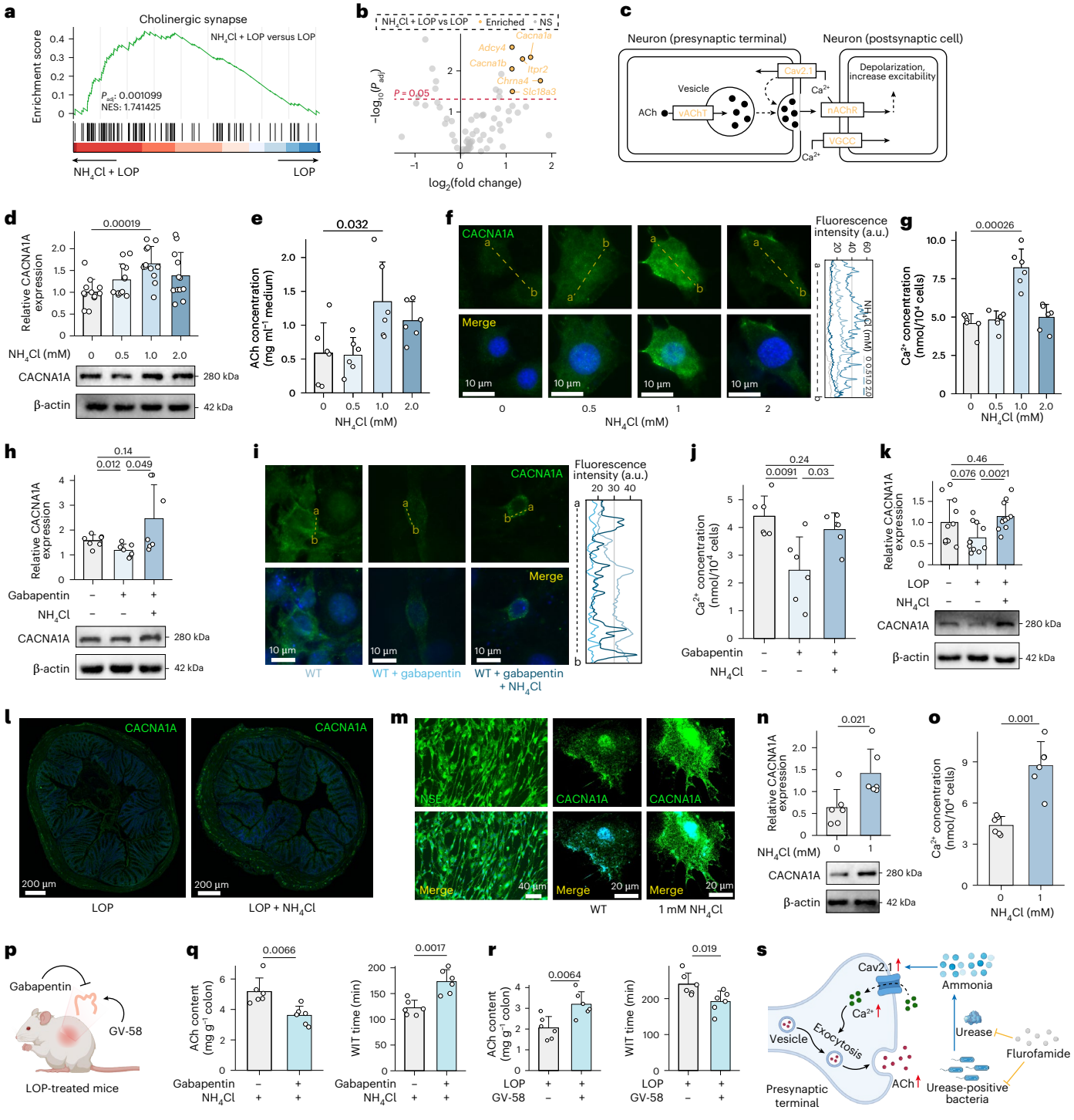
To investigate the mechanism underlying ammonia-induced ACh elevation, we performed RNA-sequencing on colon tissues from LOP-treated mice supplemented with NH_4Cl. Gene set enrichment analysis (GSEA) revealed significant enrichment of the 'cholinergic synapse' pathway, associated with ACh release (Fig. 4a). Differential expression analysis identified six significantly altered genes (*adcy4*, *cacna1a*, *cacna1b*, *chrna4*, *itpr2*, *slc18a3*), primarily related to voltage-gated Ca^{2+} channels (VGCCs), ACh transport (vesicular acetylcholine transporter, vAChT) and acetylcholine receptors (nAChR) (Fig. 4b,c). Notably, genes encoding VGCC proteins (*cacna1a* and *cacna1b*) were significantly upregulated. ACh is loaded into vesicles via vAChT and released into the synaptic cleft via exocytosis. ACh binding to postsynaptic nAChRs causes depolarization and excitation. VGCCs facilitate Ca^{2+} influx, accelerating exocytotic ACh release. As the pore-forming subunit, CACNA1A (Cav2.1 channel) mediates Ca^{2+} influx and may play a key role in ammonia-induced ACh elevation.

To elucidate the crucial role of CACNA1A, we examined the interaction between ammonia and CACNA1A protein expression in vitro. In HEK293FT cells, 1 mM NH_4Cl produced the strongest increase in CACNA1A protein abundance and more than doubled ACh release into the culture supernatant (Fig. 4d,e). Importantly, this concentration is

Fig. 4 | NH_4Cl enhances ACh levels by upregulating Cav2.1 channel expression. **a**, GSEA of colonic tissue transcriptomes from LOP-treated mice with or without NH_4Cl co-intervention. *P* value estimation is based on an adaptive multilevel split Monte Carlo scheme (FGSEA method) with Benjamini–Hochberg correction. **b**, Differential gene expression analysis within the KEGG cholinergic synapse pathway. Statistical comparisons were conducted using unpaired two-tailed Student's *t*-test with Benjamini–Hochberg correction. **c**, Schematic localization of proteins encoded by representative differentially expressed genes within the cholinergic synapse. **d**, Bottom: immunoblot analysis of CACNA1A expression in HEK293FT cells exposed to varying NH_4Cl concentrations. Top: quantification of CACNA1A levels normalized to β-actin ($n = 12$ per group). **e**, ACh content in supernatant from cells ($n = 6$ per group). **f**, Left: representative immunofluorescence images of CACNA1A (green) and DAPI (blue) in NIH3T3-L1 cells under different NH_4Cl concentrations. Right: quantification of CACNA1A fluorescence intensity. **g**, Intracellular Ca^{2+} concentration in NIH3T3-L1 cells treated with NH_4Cl ($n = 6$ per group). **h**–**j**, CACNA1A expression in cells with or without NH_4Cl or gabapentin intervention: **h**, Immunoblot analysis of CACNA1A and β-actin in HEK293FT cells ($n = 7$ per group) with quantification of the CACNA1A/β-actin ratio. **i**, Left: CACNA1A immunofluorescence (green) and DAPI (blue) in NIH3T3-L1 cells. Right: fluorescence intensity quantification. **j**, Intracellular Ca^{2+} levels in NIH3T3-L1 cells ($n = 6$ per group). **k**, Immunoblot analysis of CACNA1A expression in colonic tissue from LOP-treated mice with or without NH_4Cl intervention ($n = 11$ per group). **l**, Representative immunofluorescence staining of CACNA1A in mouse colon tissues following NH_4Cl intervention. **m**, Representative immunofluorescence images of CACNA1A (green) and DAPI (blue) in primary colonic neurons under 1 mM NH_4Cl. The image on the left shows the identification of primary colon neurons by neuron-specific enolase (NSE) immunofluorescence staining. **n**, Immunoblot analysis of CACNA1A and β-actin in primary colonic neurons ($n = 6$ per group), with quantification of the CACNA1A/β-actin ratio. **o**, Intracellular Ca^{2+} concentration in primary colonic neurons treated with 1 mM NH_4Cl ($n = 6$ per group). **p**, Experimental design for gabapentin or GV-58 administration to LOP-treated mice. **q**, WIT time and ACh content in NH_4Cl-treated mice with or without gabapentin co-intervention ($n = 6$ per group). **r**, WIT time and ACh content in LOP-treated mice administered with CACNA1A agonist GV-58 ($n = 6$ per group). **s**, Proposed mechanistic model: urease-positive isolate *L. fusiformis* elevates colonic ACh levels via ammonia-dependent upregulation of Cav2.1. Data represent mean ± s.d. of at least three biologically independent experiments. NS, not significant. Statistical significance was assessed using two-tailed Student's *t*-test. Illustrations created in BioRender: **p**, Chen, H. https://biorender.com/foe3u8n (2026); **s**, Chen, H. https://biorender.com/r95b7w9 (2026).

https://doi.org/10.1038/s41564-026-02269-8

comparable to physiological faecal ammonia levels (~0.9 mM) observed in LOP-treated mice following 60 mg kg^{-1} NH_4Cl administration (Extended Data Fig. 8c,d). Furthermore, immunofluorescence localization and intensity measurements in NIH3T3-L1 cells revealed that 1 mM NH_4Cl enhanced CACNA1A localization intensity at the plasma membrane and was accompanied by increased intracellular Ca^{2+} concentration, confirming that CACNA1A responds to NH_4Cl intervention (Fig. 4f,g). To further validate this mechanism, we employed gabapentin (VGCC inhibitor), a structural analogue of gamma-aminobutyric acid that selectively binds VGCCs, reduces Ca^{2+} influx and inhibits excitatory neurotransmitter release. While gabapentin blocked Cav2.1 channel function, NH_4Cl intervention still upregulated Cav2.1 protein levels in cells (Fig. 4h). Simultaneously, immunofluorescence indicated that NH_4Cl restored Cav2.1 fluorescence intensity and Ca^{2+} signalling to normal levels (Fig. 4i,j). These results suggest that NH_4Cl promotes Ca^{2+} influx via a pathway involving increased Cav2.1 protein abundance, thereby triggering ACh release. To confirm physiological relevance, we extended our analysis to colonic tissues and primary enteric neurons. Immunofluorescence of colonic tissues from LOP-treated mice showed that NH_4Cl markedly increased Cav2.1 expression in the myenteric muscle layer (Fig. 4l). Primary colonic neurons isolated from mice similarly showed strong upregulation of Cav2.1 protein after NH_4Cl exposure, confirmed by western blotting and immunofluorescence (Fig. 4m,n). Correspondingly, intracellular Ca^{2+} levels in these primary neurons increased significantly after NH_4Cl exposure, demonstrating functional enhancement of Ca^{2+} influx through Cav2.1 activation (Fig. 4o).



Consistently, NH_4Cl intervention significantly increased CACNA1A levels in colon tissue in vivo (Fig. 4k).

To definitively test whether Cav2.1-dependent Ca^{2+} influx mediates ammonia-induced ACh release in vivo, we performed agonist and inhibitor interventions in LOP mice (Fig. 4p). GV-58, a selective agonist for N-type and P/Q-type VGCCs, increases Ca^{2+} influx to promote presynaptic neurotransmitter release. Results showed that NH_4Cl intervention significantly shortened the WIT time and markedly increased colonic ACh content in LOP mice receiving gabapentin (Fig. 4q), effects similar to those observed in LOP mice treated with the agonist GV-58 (Fig. 4r). These results identify Cav2.1 as the key effector through which ammonia enhances colonic ACh levels, demonstrating that ammonia promotes ACh release by upregulating Cav2.1 expression and thereby increasing Ca^{2+} influx.

Discussion

Intestinal microbiota modulates ENS activity and intestinal motility through multiple pathways[15,16]. However, how microbiota-derived metabolites specifically regulate neuronal excitability and peristalsis remains unclear. Using a LOP-deficiency-induced dysmotility model, we show that urease-positive bacteria increase urea hydrolysis in response to host pathology, producing ammonia. This microbiota-derived ammonia upregulates the presynaptic Cav2.1 in enteric neurons, enhances Ca^{2+} influx and promotes ACh release, thereby restoring intestinal motility (Fig. 4s). These findings uncover a previously unrecognized microbiota–ENS regulatory mechanism and highlight microbial metabolic compensation as a fundamental strategy for maintaining motor homeostasis.

The gut microbiome, a complex community coexisting with the host, exhibits remarkable metabolic plasticity in response to physiological perturbations[17]. Here we identified a compensatory mechanism in which impaired intestinal ACh signalling triggers urease-positive bacteria to upregulate urease activity, increasing ammonia production to sustain peristalsis. *L. fusiformis* was used as a representative strain due to its robust and inducible urease activity under acidic conditions, rather than as a prevalent gut species or probiotic candidate. Metagenomic surveys indicate that *L. fusiformis* is present at low abundance in the general human population, suggesting that this mechanism is generalizable to other urease-positive taxa rather than dependent on a single strain. Mechanistically, the early decrease and subsequent rebound in colonic pH following LOP treatment, together with enhanced urease activity under acidic conditions, indicate that transient luminal acidification serves as a physiological cue for bacterial activation.

Ammonia has traditionally been considered a neurotoxic waste product, with excessive accumulation causing hyperammonemia and central nervous system damage[18]. In our study, however, we show that locally produced, microbiota-derived ammonia, not urea, is the key metabolite regulating enteric neural activity. Administration of 60 mg kg^{-1} NH_4Cl increased colonic ACh levels and accelerated whole-gut transit without raising systemic ammonia to toxic levels or causing detectable cognitive impairment. These results align with previous work showing that enteric glial cells sense local ammonia increases and modulate colonic neuromuscular transmission via GABA release, a mechanism conserved across human, pig and mouse tissue[11]. These findings highlight the context-dependent role of ammonia: at physiological levels, it enhances enteric neurotransmission, while excessive concentrations are neurotoxic, similar to nitric oxide[19]. The threshold for ammonia toxicity varies across species and individuals, emphasizing the importance of local concentrations and careful consideration in translational applications. Importantly, microbial ammonia alone cannot fully reverse chronic constipation. Structural and functional limitations of the gut, such as reduced enteric neurons, loss of interstitial cells of Cajal and impaired smooth muscle function, constrain short-term neurochemical compensation and limit full recovery[20–22].

Our study further identifies Cav2.1 as the primary effector of ammonia-mediated motility regulation. Ammonia upregulates Cav2.1, promoting presynaptic Ca^{2+} influx and enhancing ACh release to drive neurotransmission and smooth muscle contraction, consistent with Cav2.1's established role in neuromuscular signalling[23]. Beyond Cav2.1, ammonia influences intracellular Ca^{2+} and pH homeostasis, triggering Ca^{2+}- and cAMP-dependent pathways that regulate gene transcription. For example, ammonium increases *Cacna1c* expression and Ca^{2+} signalling in astrocytes, modulates neuronal excitability and vesicle release, and elevates intracellular cAMP by adenylate cyclase activation or reducing efflux[24–26]. Voltage-gated calcium channels (Cav1 and Cav2 families) are further modulated by cAMP/PKA-mediated phosphorylation, providing a plausible basis for the coordinated upregulation of *adcy4*, *cacna1a*, *cacna1b*, *chrna4*, *itpr2* and *slc18a3* in enteric neurons and glial cells[27]. Similar mechanisms may underlie ammonia-dependent regulation in glial cells, as elevated luminal ammonia has been shown to trigger Ca^{2+}-driven GABA release from enteric glia[11]. Future studies should clarify how ammonia affects Cav2.1 trafficking, endocytic recycling and post-translational modifications, which will deepen our mechanistic understanding of how microbial nitrogen metabolism sustains enteric neurotransmission and motility.

In conclusion, our study identifies a microbiota-driven compensatory mechanism in which urease-positive bacteria sustain intestinal motility by ammonia-mediated elevation of colonic ACh. The prevalence of urease-positive taxa in the human gut suggests that this mechanism is broadly relevant beyond any single strain. By linking microbial nitrogen metabolism to enteric neural signalling, our work highlights microbiota–neurotransmitter interactions and identifies promising microbial and metabolic targets for the treatment of intestinal dysmotility disorders.

Methods

Mice and housing conditions

Specific-pathogen-free (SPF) Kunming mice and SD rats (7-week-old male) were used in this study. Mice were sourced from Hunan Sleek Jingda (Changsha, China) and housed under controlled temperature (25 ± 5 °C), humidity (60%–70%) and light (12/12-h light/dark cycle) with ad libitum access to water and standard chow. All procedures were conducted in accordance with the National Institutes of Health Guide for the Care and Use of Laboratory Animals and were approved by the Institutional Ethics Committee for Animal Procedures of the Central South University (CSU-2024-0315).

Construction and evaluation of mice model of intestinal dysmotility

Intestinal dysmotility was induced in Kunming mice via intragastric loperamide (LOP, R021029, RHAWN) administration at 20 mg kg^{-1} body weight in 0.2 ml phosphate buffered saline (PBS) daily for 4 days. Gastrointestinal motility was assessed in vivo. Mice were euthanized by cervical dislocation. Colonic contents were collected and snap frozen for ammonia and urease activity measurements. Colon tissues were also snap frozen for subsequent ACh measurements.

Assessment of intestinal motility in vivo

Intestinal motility in mice was assessed using four metrics: WIT time, SIT rate, stool consistency and bead expulsion test. Detailed procedures are described below.

WIT time. Methylcellulose red dye solution was prepared by dissolving 0.2 g methylcellulose and 0.6 g carmine red (Macklin) in 10 ml PBS. Mice were gavaged with 0.2 ml of this solution and individually housed. Faeces were checked on white paper for red dye, and WIT was defined as the time from gavage to first red-coloured faecal excretion, with a maximum of 8 h.

SIT rate. Mice were gavaged with 0.2 ml of Indian ink (Biosharp) and killed 30 min later. The gastrointestinal tract was removed and straightened, and the small intestine length and ink progression distance were measured. SIT was calculated as the ratio of ink progression to total small intestine length. Mice were fasted for 24 h before the experiment, with water being made available ad libitum[28].

Stool consistency. Stool consistency was assessed on the basis of the Bristol stool scale and faecal water content. Faeces were collected within 2 h, weighed, dried at 100 °C for 1 h, and moisture content calculated as: 'Faecal moisture content = (wet weight of faeces−dry weight of faeces)/wet weight of faeces'. Stool appearance, shape and consistency were scored according to the Bristol scale.

Bead expulsion test. To evaluate colorectal propulsion, mice were lightly anaesthetized with isoflurane, and a 3-mm glass bead was inserted 2 cm into the distal colon. Mice were then placed in individual cages to recover, and the time to bead expulsion was recorded[29].

Sample collection

Faecal samples were collected 1 day before killing via gentle anal stimulation with sterile cotton swabs, snap frozen in liquid nitrogen and stored at −80 °C. Blood was collected from the orbital veins under isoflurane anaesthesia before euthanasia by cervical dislocation and stored at −80 °C. Colonic contents were obtained by gentle compression, snap frozen and stored at −80 °C. Colon tissues were washed with PBS and processed according to the specific biochemical assays to be performed.

Drug preparation and animal intervention

Drugs and their administration protocols are summarized below. Specifically, ACh (Macklin) was diluted in PBS and orally gavaged (10 mg kg^{-1} body weight, 0.2 ml per mouse daily for 2 consecutive days). FFA (Ambeed) was dissolved in 0.1% dimethylsulfoxide/PBS and administered intraperitoneally (i.p.) at 6 mg kg^{-1}. NH_4Cl (Sinopharm) was dissolved in PBS and gavaged at 15, 30, 60 and 120 mg kg^{-1} body weight. Gabapentin (T0702, TargetMol) and GV-58 (T11517, TargetMol) were dissolved in PBS and administered i.p. at 50 mg kg^{-1} (gabapentin) and 50 μM (GV-58). L-glutamine (Gln) (Macklin) was dissolved in PBS at 100 mg ml^{-1} and orally gavaged at 0.2 ml per mouse. Unless specified, PBS was used as the vehicle, and all doses were normalized to body weight. Drug solutions were administered at a uniform volume of 0.2 ml per dose.

Quantitative measurement and characterization of biochemical parameters

ACh levels were measured using the acetylcholine assay kit (A105-1-1 and A105-2-1, NJJCBIO). Faecal ammonia was assessed by indophenol blue colorimetry. Briefly, 5.0 ml solution A (5.0 g phenol, 2.0 ml 1.25% (w/v) $Na_2[Fe(CN)_5NO]{\cdot}2H_2O$ in 500 ml water) and 5.0 ml solution B (2.5 g NaOH, 2.0 g trisodium citrate, 3.5 ml NaClO in 500 ml water) were mixed with 100 μl of sample and incubated at 37 °C for 20 min. Absorbance at 637 nm was measured and ammonia levels calculated using a standard curve prepared from $(NH_4)_2SO_4$. Blood ammonia levels were quantified using the Blood Ammonia Content Assay kit (BC4385, Solarbio). Faecal urease activity was determined with the Urease (UE) Activity Assay kit (BC4115, Solarbio). Intracellular Ca^{2+} concentration was quantified using the Fluo-4, AM Calcium Ion Concentration Assay kit (CA1190, Solarbio). Urea content was quantified using the Urea Nitrogen/Urea Content Assay kit (BC1535, Solarbio). Arginase activity was quantified using the Arginase Activity Assay kit (BC5550, Solarbio). Glutamine content was quantified using the Glutamine (Gln) Content kit (G0429W96, Suzhou Grace Biotechnology). The activity of glutamine synthetase was quantified using Glutamine Synthetase (GS) Activity Assay kit (BC0910, Solarbio). All assays were performed according to manufacturer protocols.

Incubation of faecal microbiota with LOP in vitro

To evaluate the direct effects of LOP on gut microbiota, fresh faecal samples from healthy donors were homogenized under anaerobic conditions in pre-reduced PBS (pH 7.4). Homogenates (10% v/v) were inoculated into brain heart infusion (BHI) medium supplemented with PBS (control) or LOP (final concentration 50 μM) and incubated at 37 °C for 24 h under anaerobic conditions. After incubation, urease activity was measured according to manufacturer instructions, and bacterial pellets were collected for DNA extraction and 16S rRNA gene sequencing.

16S rRNA gene sequencing and analysis

To assess compositional changes in gut microbiota in vivo and the direct effects of LOP in vitro, total genomic DNA was extracted from mice faeces and bacterial pellets were cultured using the OMEGA Soil DNA kit (Omega Bio-Tek). The V3 and V4 regions of the 16S rRNA gene were sequenced on the Illumina NovaSeq PE250 platform (Shanghai BIOZERON Biotechnology). Raw reads were processed using QIIME2 for quality control and annotated using the feature-classifier and classify-consensus-blast plugins against the Silva database[30]. Taxonomic classification was performed. Alpha and beta diversity (Bray–Curtis distance) were analysed using the 'vegan' package in RStudio[31].

Metagenomic sequencing and analysis of faecal samples

To evaluate changes in the functional gene of the gut microbiome in LOP-treated mice, total genomic DNA of mice stool samples was extracted using the OMEGA Soil DNA kit (Omega Bio-Tek). DNA libraries (400 bp inserts) were prepared using the NEXTFLEX Rapid DNA-Seq kit and sequenced on the Illumina HiSeq X-ten platform (PE150) (Shanghai BIOZERON). Raw reads were quality filtered using Fastp, Bowtie2 and Fastuniq, and assembled into contigs using Megahit[32–35]. Taxonomic classification was annotated using Kraken2 and normalized with Bracken[36,37]. Functional genes were predicted using Prodigal, redundancy removed by CD-HIT, coverage estimated with Salmon, and functional annotation performed with eggNOG-mapper[38–41]. KEGG pathways and urease-related differential genes were analysed using the Mann–Whitney *U*-test with false discovery rate correction. The bacterial hosts that contribute *ure* gene were identified using Kraken2. Genes related to the synthesis and degradation of Gln, choline and ACh were curated using KEGG database keyword searches.

Analysis of public faecal metagenome and metabolome datasets for the constipated cohort

To evaluate gut microbiome composition and function in individuals with intestinal dysmotility, faecal metagenomic data were retrieved from NCBI (accession numbers: PRJNA779475, GSE113540)[42,43]. Following quality control, assembly and functional annotation (as described in 'Metagenomic sequencing and analysis of faecal samples'), urease abundance was quantified. Concurrently, ammonia-related metabolite data associated with constipation were obtained from the Gut Microbial Metabolite Association with Disease (GMMAD) database[44]. Patient metadata in GMMAD do not include information on previous drug or laxative use.

Temporal dynamics of colonic ACh, luminal pH and faecal ammonia

To investigate the progression of intestinal dysmotility, mice were divided into two groups: PBS and LOP. LOP (0.2 ml) or PBS was administered daily via gavage. Five mice per group were euthanized daily by cervical dislocation, and colonic tissue and contents were collected on ice. Luminal pH was measured immediately using a pH metre with an electrochemical probe (Sartorius). Remaining colonic contents were snap frozen for ammonia quantification, and tissue samples were snap frozen for subsequent ACh measurement.

Quantitative PCR

To assess the abundance of urease-positive bacterial isolates and the changes in urease gene expression, qPCR was performed. Genomic DNA was extracted from faeces using the Universal Genomic DNA Extraction kit (D2100, Solarbio). Total RNA was isolated using Trizol (SK1312; Sango) and reverse transcribed into cDNA using the AMV First Strand cDNA Synthesis kit (SK2445, Sango). Six representative urease-positive isolates were analysed. Primers targeting the *ureC* gene and the universal 16S rRNA gene were designed on the basis of conserved regions (Supplementary Table 4). Real-time PCR was conducted using the Takara SYBR Green PCR Master Mix (RR820A, Takara) on an SLAN-96S real-time PCR system (Honshi). Relative ureC expressions was normalized to 16S rRNA using the $2^{-\Delta\Delta C_t}$ method.

Collection of faecal samples from volunteers

To isolate urease-positive bacteria, faecal samples from volunteers ($n = 3$) with intestinal motility disorders were collected (Supplementary Table 3). Intestinal motility disorders were defined as: fewer than three spontaneous bowel movements per week, excessive straining during defecation, and Bristol Stool Scale score <3. Volunteers provided written informed consent, and patient information was anonymized. Exclusion criteria included the use of laxatives, probiotics, antidiarrheals, glucocorticoids, immunosuppressants, antitumour agents or antibiotics. Experiments were reviewed and approved by the Institutional Review Board of the School of Basic Medical Science of Central South University (No. 2021-KT75).

Isolation and identification of urease-positive bacteria

To screen urease-positive bacteria specifically, faecal suspensions were prepared in PBS, settled for 5 min, and the supernatant plated on urea phenol red (UPR) agar. Colonies inducing a red colour change were streaked onto fresh UPR agar for purification through three successive passages. Individual colonies were identified by full-length 16S rRNA gene amplification using universal primers (Supplementary Table 4), Sanger sequencing and taxonomic assignment via BLASTn against NCBI RefSeq. All isolates were stored at −80 °C in glycerol stocks.

Antibiotic treatment, cultivation and intervention of *L. fusiformis*

Mice received a 7-day broad-spectrum antibiotic (Abx) cocktail (vancomycin 0.5 mg ml^{-1}, ampicillin 1 mg ml^{-1}, metronidazole 1 mg ml^{-1}, neomycin sulfate 1 mg ml^{-1}) (Shanghai Macklin) in drinking water to reduce gut microbiota. *L. fusiformis* isolated from human faeces were cultured in 5.0 ml of lysogeny broth (LB) medium (37 °C, 200 r.p.m., 12 h) to prepare bacterial suspensions. Abx-treated mice were gavaged with 0.2 ml of suspension. Urease activity of *L. fusiformis* under different pH conditions (pH 5 and 7) was assessed after 24 h culture.

Hematoxylin and eosin staining and histopathological scoring

To assess whether *L. fusiformis* intervention caused damage to the colonic tissue, histopathological analysis was performed. Colon tissues were rinsed with PBS, fixed in 4% paraformaldehyde and subjected to hematoxylin and eosin staining. Section images were captured using the NanoZoomer S360 imaging system, and histopathological scoring was performed.

Whole-genome sequencing and analysis of *L. fusiformis*

To characterize the presence of genes encoding urease in *L. fusiformis*, whole-genome sequencing on *L. fusiformis* was performed. Genomic DNA (3 µg) of *L. fusiformis* were used to construct a paired-end library (insert size 400 bp) following Illumina protocols. Sequencing was performed on the Illumina NovaSeq 6000 platform (Shanghai Biozeron). Raw reads were quality controlled using Fastp and assembled using SPAdes and MetaBAT2 (refs. 45,46). Genome annotation with Prokka identified urease-coding genes[47].

Construction and validation of recombinant *E. coli* BL21 expressing *L. fusiformis* urease

To explore the role of urease in promoting ACh release, urease genes (*ureA*, *ureB*, *ureC*) identified from *L. fusiformis* whole-genome sequencing were heterologously expressed in *E. coli* BL21 (DE3) (B528414, Sangon Biotech). Specifically, *ureA* and *ureC* were cloned into pETDuet-1 (VT1237, YouBio) and *ureB* into pET-28a (VT1207, YouBio) (Supplementary Table 4). Recombinant constructs were transformed into *E. coli* BL21 (DE3), and ten colonies were randomly selected for PCR verification of plasmid coexistence using gene-specific primers. Plasmid copy numbers were quantified by qPCR (Supplementary Table 4).

Assessment of plasmid stability under antibiotic-free conditions

To evaluate stability without antibiotic selection, recombinant BL21 strains were serially passaged in antibiotic-free LB for 40 generations. Samples from generations 0, 20 and 40 were plated on non-selective and dual-antibiotic LB agar plates, and the proportion of colonies retaining both plasmids was determined. In vivo stability was assessed by collecting faeces from mice before, during and after oral administration, followed by qPCR quantification of plasmid abundance (Supplementary Table 4).

Verification of urease expression and nickel-dependent activity

Recombinant BL21 strains were induced with 0.5 mM IPTG for 4 h at 30 °C. Bacterial pellets were washed with PBS and used for gavage or downstream assays. Urease activity was measured using a phenol-hypochlorite assay with or without 1 mM Ni^{2+} to assess Ni^{2+}-dependent activation. Expression of all three urease subunits was confirmed by Tris-tricine SDS–PAGE followed by in-gel digestion and high-resolution LC–MS analysis (Orbitrap Astral–Vanquish NEO, BIORUN BIOSCIENCES)

In vivo administration of recombinant BL21 and evaluation of functional activity

IPTG-induced recombinant BL21+Lf-ureABC or empty-vector controls were orally administered to mice twice daily for 4 days. Faecal urease activity and ammonia levels were measured using commercial kits. Functional effects were assessed in LOP-induced mice by measuring colonic ACh concentrations and intestinal transit as described above.

Assessment and analysis of cognitive and memory abilities

Elevated levels of ammonia in the body can impair cognitive function in the host. To assess the impact of ammonia intervention on host cognition, mice underwent Y-maze, novel object recognition and Morris water maze tests. The specific experimental procedures are described below.

Y-maze. Rodents exhibit innate novelty-seeking behaviour, which the Y-maze apparatus utilizes to assess exploratory drive. The maze consists of three identical arms symmetrically radiating from a central junction in a Y-shaped configuration. During testing, mice were gently positioned at the central junction facing a standardized starting orientation. Exploratory behaviour was video recorded under controlled environmental conditions for 8 min per trial. Entry into an arm was counted when a mouse moved all four limbs into the arm. Arm entry sequences were quantified, with three sequential entries into distinct arms constituting a complete alternation event. The spontaneous alternation percentage was calculated as:

$$\text{Alternation rate}(\%) = [\text{Number of alternations}/(\text{Total arm entries} - 2)] \times 100\% \quad (1)$$

The subtraction of 2 accounts for initial entries before the first possible alternation sequence.

Novel object recognition. The novel object recognition test was conducted in an opaque open-field arena. Two identical sample objects (A1, A2) and one novel object (B) were utilized. Day 1 (familiarization phase): Identical objects (A1, A2) were positioned in adjacent corners. Subjects were gently placed at the arena centre avoiding directional bias. Testing occurred in a sound-attenuated room with blackout curtains to minimize external interference. Exploratory behaviour was video recorded for 10 min to quantify locomotion trajectories and object interaction time. Subjects were subsequently returned to home cages. Day 2 (test phase): The less familiar object was replaced with the novel object (B) while maintaining identical spatial configuration. Subjects underwent an identical 10-min trial. Exploration time for both the retained familiar object (A) and the novel object (B) was recorded.

Morris water maze. The Morris water maze evaluates spatial learning and memory in rodents. The apparatus consists of a circular opaque pool (150 cm diameter × 50 cm height) filled with water maintained at 22–24 °C. Titanium dioxide was added to render the water opaque. A hidden escape island was submerged 1 cm below the water surface in one quadrant. Distal visual cues surrounded the pool to facilitate spatial navigation. Testing was divided into the acquisition phase (days 1–4) and the probe test (day 5). For the acquisition phase: subjects underwent three daily trials (60 s per trial) with ≥30 min inter-trial intervals; starting positions varied pseudorandomly across non-target quadrants; successful platform localization was defined as remaining on the platform for ≥3 s; subjects failing to locate the platform within 60 s were guided to it and remained for 20 s; the primary metric was the mean escape latency across daily trials. For the probe test: the platform was removed; subjects were released from the quadrant diametrically opposite to the original platform location; platform-site crossings during a 60 s trial were quantified.

Assessment of colonic motility in vitro

To evaluate colonic motility in vitro, contractile activity and CMMCs were assessed using an organ bath system. The detailed experimental procedure is described below.

Colonic contractility. Organ bath experiments were performed in Krebs buffer (composition in mmol l^{-1}: 117 NaCl, 4.7 KCl, 2.5 $CaCl_2$, 1.2 $MgCl_2$, 1.2 NaH_2PO_4, 25 $NaHCO_3$, 11 glucose). The colon tissue obtained from killed mice was immediately immersed in pre-configured Krebs buffer at 37 °C. Longitudinal colonic strips were mounted in organ chambers filled with Krebs buffer, with one end connected to an isometric force transducer (MD3000-C, Zhenghua Biotech). Electrical field stimulation (EFS) was delivered via parallel platinum electrodes coupled to an MD3000-C Bio-Signal Acquisition System (Zhenghua Biotech). Tissues were equilibrated for 20 min under 0.5 g resting tension. Isometric contractile responses were recorded and analysed using the MD3000-C Multi-Channel Physiological Signal Acquisition system.

CMMCs. The experiments were conducted following established protocols. Briefly, the colon was mounted in an organ bath experiment, and its lumen was filled with oxygenated Krebs buffer. The entire solution and lumen were continuously perfused with a carbogen gas mixture (95% O_2 and 5% CO_2). Following an equilibration period, colonic contractile activity was recorded using a professional camera (Sony) positioned above the tissue. Spatiotemporal maps along the proximal–distal axis of the colon were generated using MATLAB (R2025a) to quantify the frequency and velocity of CMMCs.

In situ vascular cannulation and measurement of ACh

To evaluate ammonia-induced ACh release in vivo, SD rats were anaesthetized with pentobarbital sodium (40 mg kg^{-1}, i.p.), and the abdominal aorta and inferior vena cava were exposed via midline incision. Polyethylene catheters were inserted into the abdominal aorta for infusion and the inferior vena cava for venous blood collection. Pre-warmed solution of 1 mM NH_4Cl was infused at 0.2 ml min^{-1} using a peristaltic pump, and venous effluents were collected for 3–5 min for ACh quantification. At the end of perfusion, colonic tissues were rapidly excised and snap frozen in liquid nitrogen for ACh quantification.

RNA-seq and transcriptomic analysis of colonic tissues

To elucidate the underlying mechanisms of the colonic response to ammonia intervention, total RNA was extracted from colonic tissue using TRIzol reagent (Invitrogen) and treated with DNase I (TaKara). RNA integrity and concentration were assessed with an Agilent 2100 Bioanalyzer and a NanoDrop ND-2000 spectrophotometer. For library construction, 1 μg of DNase-treated total RNA was processed using the Illumina TruSeqTM RNA Sample Preparation kit. Polyadenylated mRNA was enriched by oligo(dT) beads and chemically fragmented. Subsequent steps included cDNA synthesis, end repair, adenylation and ligation of indexed adapters. Target cDNA fragments (200−-300 bp) were size selected in 2% Low Range Ultra Agarose and amplified for 15 cycles using Phusion DNA Polymerase (NEB). After quantification with TBS380, paired-end sequencing was performed by BIOZERON. Raw reads were quality filtered with Fastp, aligned to the GRCm39 reference genome using Hisat2 and analysed for differential expression with DESeq2 (ref. 48). GSEA was performed using the 'clusterProfiler' R package[49]. Gene functions were determined in the KEGG database (https://www.kegg.jp/kegg/).

Cell lines and primary cells

HEK293FT cells were kindly provided by Professor Gang Yin's Lab (Central South University). NIH3T3 mouse embryonic fibroblasts (ATCC CRL-1658) were obtained from Geneline Bioscience (GL0021). Primary mouse colonic neurons were purchased from Cellverse Biosciences (MIC-iCell-d021), and neuronal identity was confirmed by neuron-specific enolase immunofluorescence. Cells were maintained in DMEM medium supplemented with 10% bovine calf serum and 1% penicillin/streptomycin at 37 °C in 5% CO_2.

Western blot

To investigate the expression of Cav2.1 in cells after ammonia treatment, cells were washed with PBS and lysed on ice for 30 min in RIPA buffer (Beyotime) with protease inhibitors. Lysates were centrifuged at 12,000 × *g* for 10 min at 4 °C and supernatants collected. Proteins were denatured in 5× loading buffer at 95 °C for 5 min, resolved on 10% Tris-glycine SDS–PAGE and transferred to PVDF membranes. Membranes were blocked with 5% milk in Tris-buffered saline with Tween-20 (TBST) for 1 h incubated with primary antibodies (CACNA1A, rabbit, 1:1,000, db16079, Diagbio) overnight at 4 °C. After three 5-min TBST washes, HRP-conjugated secondary antibodies (goat anti-rabbit IgG or goat anti-mouse IgG, 1:5,000 dilution, Bioss) were applied for 1 h at room temperature. Immunoreactive bands were detected using enhanced chemiluminescence (Ultra ECL, Biosharp) and quantified using ImageJ. β-actin (1:1,000, 66009-1-Ig, Proteintech) served as loading control.

Cellular immunofluorescence staining

To determine the subcellular localization of Cav2.1 in cells after ammonia treatment, immunofluorescence staining was performed. Cells in 24-well plates were fixed with 4% paraformaldehyde for 15 min, permeabilized and blocked with blocking buffer (5% BSA, 10% normal goat serum, 0.3% TritonX-100 in PBS) for 1 h. Primary antibodies (CACNA1A, rabbit, 1:1,000, db16079, Diagbio) were applied overnight at 4 °C. After PBS washes, Alexa Fluor 488-conjugated goat anti-rabbit IgG (H + L) (1:5,000, A0423, Beyotime) and DAPI nuclear counterstain (C0065, Solarbio) were applied for 1 h. Slides were mounted with antifade

medium and imaged using an inverted fluorescence microscope. Fluorescence intensity was quantified with ImageJ.

Immunofluorescence staining of colon tissue

To investigate the in vivo response of Cav2.1 from colon to ammonia intervention, immunofluorescence staining on the post-treatment colon tissue was performed. Colon sections were deparaffinized and rehydrated, then antigen retrieval performed. Sections were blocked with 10% serum for 30 min, incubated with anti-Cav2.1 primary antibody (CACNA1A, rabbit, 1:100, db16079, Diagbio) overnight at 4 °C, followed by fluorochrome-conjugated secondary antibody (Alexa Fluor 488 donkey anti-rabbit IgG(H + L), 1:400, A21206, ThermoFisher) for 45 min at 37 °C. Nuclei were counterstained with DAPI and images captured with an Olympus BX53 fluorescence microscope.

Statistical analysis

Animals were randomly allocated to treatment groups and data collection was randomized. For all experiments, investigators were blinded to group allocation during data collection and analysis. Sample sizes were determined according to those used in similar studies from our group. Statistical analyses were performed using R with packages as specified earlier. Student's *t*-tests were exclusively two sided. Each data point represents an independent biological replicate. All experiments were repeated in at least three independent biological replicates.

Reporting summary

Further information on research design is available in the Nature Portfolio Reporting Summary linked to this article.

Data availability

Metagenomic sequencing data analysed during the current study are available in the Sequence Read Archive (https://www.ncbi.nlm.nih.gov/sra) under accession number PRJNA1201799. 16S rRNA gene sequencing and RNA-seq data are available in the Genome Sequence Archive (https://ngdc.cncb.ac.cn/gsa/) under accession number PRJCA042949 and CRA028483. Source data are provided with this paper.

References

1. Auteri, M. et al. GABA and GABA receptors in the gastrointestinal tract: from motility to inflammation. *Pharmacol. Res.* **93**, 11–21 (2015).
2. Ehlert, F. J., Pak, K. J. & Griffin, M. T. Muscarinic agonists and antagonists: effects on gastrointestinal function. *Handb. Exp. Pharmacol.* **208**, 343–374 (2012).
3. Burleigh, D. E. Evidence for a functional cholinergic deficit in human colonic tissue resected for constipation. *J. Pharm. Pharmacol.* **40**, 55–57 (1988).
4. Fujita, Y. et al. Microbiota-derived acetylcholine can promote gut motility in *Drosophila melanogaster*. *Phil. Trans. R. Soc. B Biol. Sci.* https://doi.org/10.1098/rstb.2023.0075 (2024).
5. Collier, C. A. et al. Crisis in the gut: navigating gastrointestinal challenges in Gulf War Illness with bioengineering. *Mil. Med. Res.* https://doi.org/10.1186/s40779-024-00547-2 (2024).
6. De Palma, G. et al. Transplantation of fecal microbiota from patients with irritable bowel syndrome alters gut function and behavior in recipient mice. *Sci. Transl. Med.* https://doi.org/10.1126/scitranslmed.aaf6397 (2017).
7. Ge, X. L. et al. Antibiotics-induced depletion of mice microbiota induces changes in host serotonin biosynthesis and intestinal motility. *J. Transl. Med.* https://doi.org/10.1186/s12967-016-1105-4 (2017).
8. Vincent, A. D. et al. Abnormal absorptive colonic motor activity in germ-free mice is rectified by butyrate, an effect possibly mediated by mucosal serotonin. *Am. J. Physiol. Gastrointest. Liver Physiol.* **315**, G896–G907 (2018).
9. Neufeld, K. A. M. et al. The microbiome is essential for normal gut intrinsic primary afferent neuron excitability in the mouse. *Neurogastroenterol. Motil.* **25**, 183–e88 (2013).
10. Mobley, H. L. & Hausinger, R. P. Microbial ureases: significance, regulation, and molecular characterization. *Microbiol. Rev.* **53**, 85–108 (1989).
11. Fried, D. E. et al. Ammonia modifies enteric neuromuscular transmission through glial γ-aminobutyric acid signaling. *Am. J. Physiol. Gastrointest. Liver Physiol.* **313**, G570–G580 (2017).
12. Wang, P. et al. Gut microbiome-derived ammonia modulates stress vulnerability in the host. *Nat. Metab.* https://doi.org/10.1038/s42255-023-00909-5 (2023).
13. Krumbeck, J. A. et al. Characterization of the ecological role of genes mediating acid resistance in *Lactobacillus reuteri* during colonization of the gastrointestinal tract. *Environ. Microbiol.* **18**, 2172–2184 (2016).
14. Schreiber, S. et al. The spatial orientation of *Helicobacter pylori* in the gastric mucus. *Proc. Natl Acad. Sci. USA* **101**, 5024–5029 (2004).
15. Obata, Y. et al. Neuronal programming by microbiota regulates intestinal physiology. *Nature* **578**, 284–289 (2020).
16. Servin-Vences, M. R. et al. PIEZO2 in somatosensory neurons controls gastrointestinal transit. *Cell* **186**, 3386–3399 (2023).
17. Bubier, J. A. et al. Host genetic control of gut microbiome composition. *Mamm. Genome* **32**, 263–281 (2021).
18. Cagnon, L. & Braissant, O. Hyperammonemia-induced toxicity for the developing central nervous system. *Brain Res. Rev.* **56**, 183–197 (2007).
19. Huang, Z. J. et al. Nitric oxide donor-based cancer therapy: advances and prospects. *J. Med. Chem.* **60**, 7617–7635 (2017).
20. Bharucha, A. E. & Lacy, B. E. Mechanisms, evaluation, and management of chronic constipation. *Gastroenterology* **158**, 1232–1249.e3 (2020).
21. Lyford, G. L. et al. Pan-colonic decrease in interstitial cells of Cajal in patients with slow transit constipation. *Gut* **51**, 496–501 (2002).
22. Rueckert, H. & Ganz, J. How to heal the gut's brain: regeneration of the enteric nervous system. *Int. J. Mol. Sci.* https://doi.org/10.3390/ijms23094799 (2022).
23. Li, Z. Q. et al. Structural basis for different ω-agatoxin IVA sensitivities of the P-type and Q-type Cav2.1 channels. *Cell Res.* **34**, 273–274 (2024).
24. Lazarenko, R. M. et al. Ammonium chloride alters neuronal excitability and synaptic vesicle release. *Sci. Rep.* **7**, 5061 (2017).
25. Riley, B. B. & Barclay, S. L. Ammonia promotes accumulation of intracellular cAMP in differentiating amoebae of *Dictyostelium discoideum*. *Development* **109**, 715–722 (1990).
26. Wang, F. et al. Ammonium increases Ca^{2+} signalling and upregulates expression of Cav1.2 gene in astrocytes in primary cultures and in the in vivo brain. *Acta Physiol.* **214**, 261–274 (2015).
27. Kobrinsky, E. Heterogeneity of calcium channel/cAMP-dependent transcriptional activation. *Curr. Mol. Pharmacol.* **8**, 54–60 (2015).
28. Zhang, C. C. et al. A key genetic factor governing arabinan utilization in the gut microbiome alleviates constipation. *Cell Host Microbe* https://doi.org/10.1016/j.chom.2023.10.011 (2023).
29. Han, M. N. et al. Assessment of gastrointestinal function and enteric nervous system changes over time in the A53T mouse model of Parkinson's disease. *Acta Neuropathol. Commun.* **13**, 58 (2025).
30. Bolyen, E. et al. Reproducible, interactive, scalable and extensible microbiome data science using QIIME 2. *Nat. Biotechnol.* **37**, 852–857 (2019).
31. Dixon, P. VEGAN, a package of R functions for community ecology. *J. Veg. Sci.* **14**, 927–930 (2003).

32. Chen, S. F. et al. fastp: an ultra-fast all-in-one FASTQ preprocessor. *Bioinformatics* **34**, 884–890 (2018).
33. Langdon, W. B. Performance of genetic programming optimised Bowtie2 on genome comparison and analytic testing (GCAT) benchmarks. *Biodata Mining* https://doi.org/10.1186/s13040-014-0034-0 (2015).
34. Li, D. H. et al. MEGAHIT: an ultra-fast single-node solution for large and complex metagenomics assembly via succinct de Bruijn graph. *Bioinformatics* **31**, 1674–1676 (2015).
35. Xu, H. B. et al. FastUniq: a fast de novo duplicates removal tool for paired short reads. *PLoS ONE* https://doi.org/10.1371/journal.pone.0052249 (2012).
36. Lu, J. et al. Bracken: estimating species abundance in metagenomics data. *PeerJ Comput. Sci.* https://doi.org/10.7717/peerj-cs.104 (2017).
37. Wood, D. E. et al., Improved metagenomic analysis with Kraken 2. *Genome Biol.* https://doi.org/10.1186/s13059-019-1891-0 (2019).
38. Fu, L. M. et al. CD-HIT: accelerated for clustering the next-generation sequencing data. *Bioinformatics* **28**, 3150–3152 (2012).
39. Huerta-Cepas, J. et al. Fast genome-wide functional annotation through orthology assignment by eggNOG-Mapper. *Mol. Biol. Evol.* **34**, 2115–2122 (2017).
40. Hyatt, D. et al. Prodigal: prokaryotic gene recognition and translation initiation site identification. *BMC Bioinformatics* https://doi.org/10.1186/1471-2105-11-119 (2010).
41. Patro, R. et al. Salmon provides fast and bias-aware quantification of transcript expression. *Nat. Methods* **14**, 417–419 (2017).
42. Dan, Z. et al. Altered gut microbial profile is associated with abnormal metabolism activity of Autism Spectrum Disorder. *Gut Microbes* **11**, 1246–1267 (2020).
43. Tian, H. L. et al. Gut metagenome as a potential diagnostic and predictive biomarker in slow transit constipation. *Front. Med.* https://doi.org/10.3389/fmed.2021.777961 (2022).
44. Wang, C. Y. et al. GMMAD: a comprehensive database of human gut microbial metabolite associations with diseases. *BMC Genomics* https://doi.org/10.1186/s12864-023-09599-5 (2023).
45. Bankevich, A. et al. SPAdes: a new genome assembly algorithm and its applications to single-cell sequencing. *J. Comput. Biol.* **19**, 455–477 (2012).
46. Kang, D. W. D. et al. MetaBAT 2: an adaptive binning algorithm for robust and efficient genome reconstruction from metagenome assemblies. *PeerJ* https://doi.org/10.7717/peerj.7359 (2019).
47. Seemann, T. Prokka: rapid prokaryotic genome annotation. *Bioinformatics* **30**, 2068–2069 (2014).
48. Kim, D. et al. Graph-based genome alignment and genotyping with HISAT2 and HISAT-genotype. *Nat. Biotechnol.* **37**, 907–915 (2019).
49. Yu, G. C. et al. clusterProfiler: an R package for comparing biological themes among gene clusters. *OMICS* **16**, 284–287 (2012).

Acknowledgements

We thank G. Shu (Professor Gang Yin's Lab, Central South University) for providing the HEK293FT cells, S. Yao (Department of Physiology, Central South University) for her assistance in analysing the histopathological slide results and Z. Zhang (Department of Spine Surgery, The Second Xiangya Hospital, Central South University) for his assistance in in situ vascular cannulation. This work was funded by the National Natural Science Foundation of China (32170071 to Z.Y. and 32300051 to J.H.), the Natural Science Foundation of Hunan Province (2025JJ50101 to Z.Y. and 2023JJ30651 to J.H.) and the Innovation-Driven Research Programme of Central South University (2023CXQD059 to Z.Y.).

Author contributions

Z.Y. designed the research. H.C., Z.W., and W.Y. completed the sample and data collection. H.C., Z.W. and Y.Z. analysed and visualized the data. H.C., Z.W. and J.H. wrote the paper draft. H.C., Z.W., Y.Z., W.Y., J.H. and Z.Y. wrote and edited the final paper. All authors contributed to the article and approved the submitted version.

Competing interests

The authors declare no competing interests.

Additional information

Extended data is available for this paper at https://doi.org/10.1038/s41564-026-02269-8.

Supplementary information The online version contains supplementary material available at https://doi.org/10.1038/s41564-026-02269-8.

Correspondence and requests for materials should be addressed to Zheng Yu.

Peer review information *Nature Microbiology* thanks Jian-Guo Chen, Karl-Herbert Schäfer and the other, anonymous, reviewer(s) for their contribution to the peer review of this work. Peer reviewer reports are available.

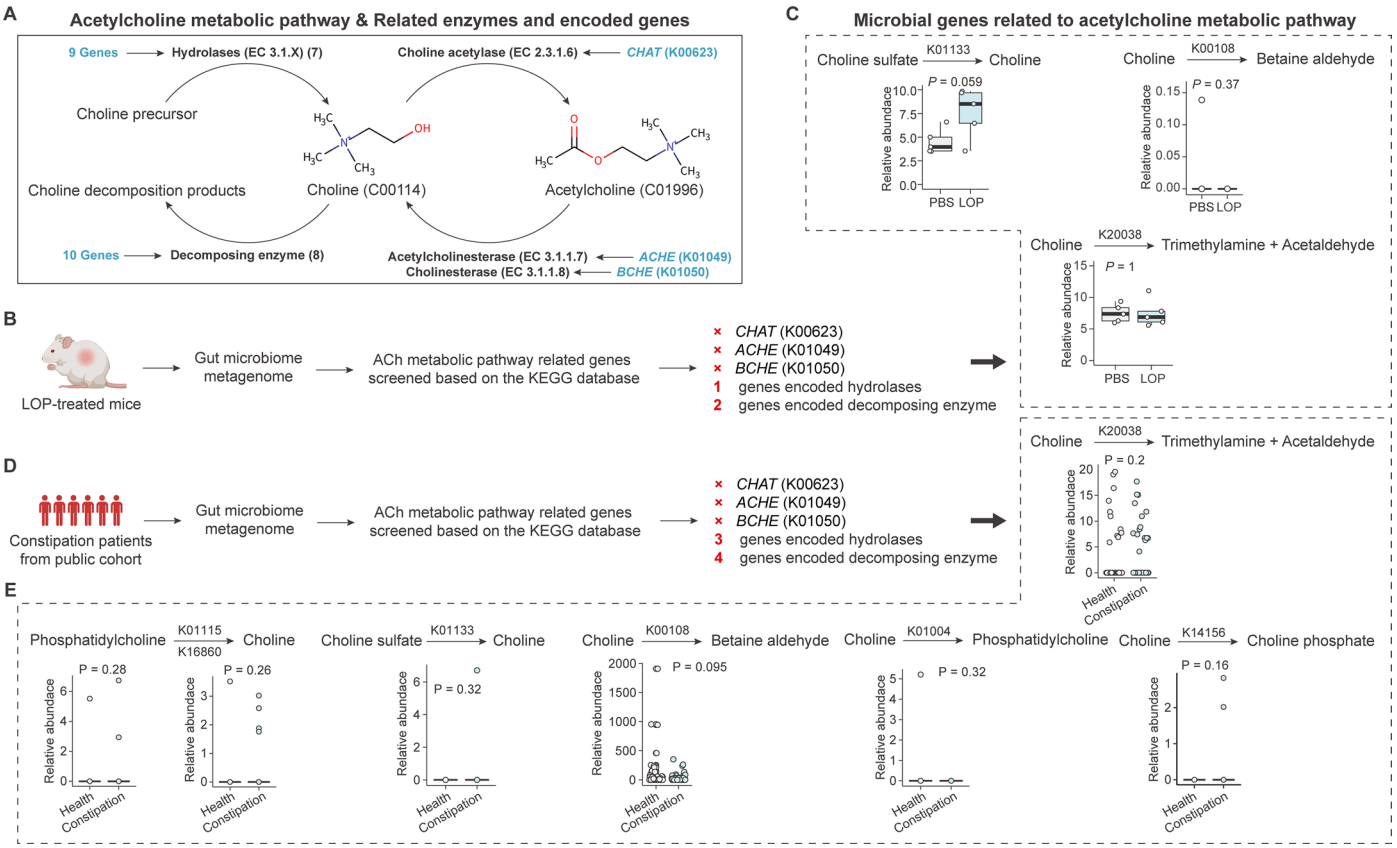
Reprints and permissions information is available at www.nature.com/reprints.

Publisher's note Springer Nature remains neutral with regard to jurisdictional claims in published maps and institutional affiliations.

Springer Nature or its licensor (e.g. a society or other partner) holds exclusive rights to this article under a publishing agreement with the author(s) or other rightsholder(s); author self-archiving of the accepted manuscript version of this article is solely governed by the terms of such publishing agreement and applicable law.

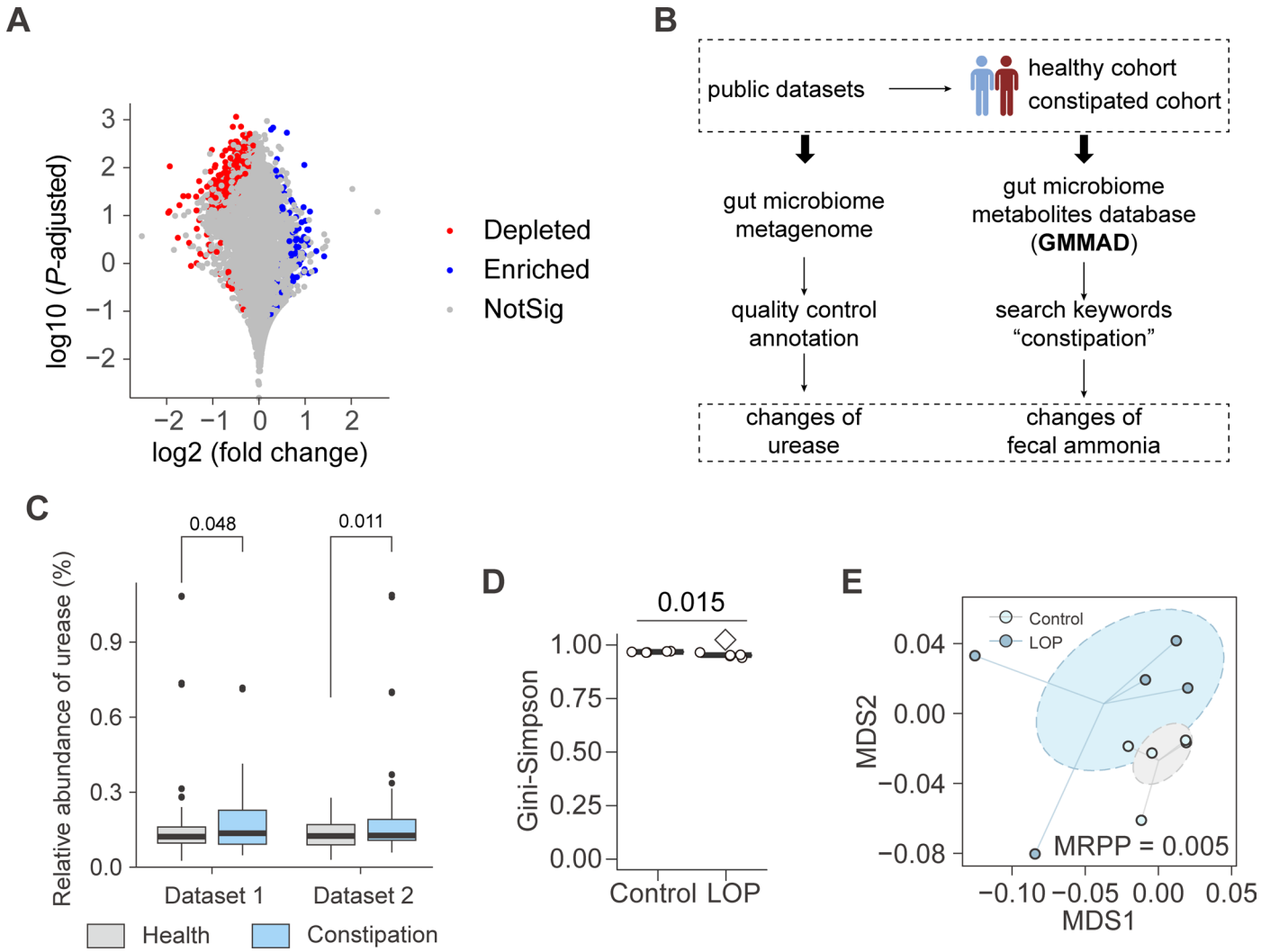
© The Author(s), under exclusive licence to Springer Nature Limited 2026

https://doi.org/10.1038/s41564-026-02269-8



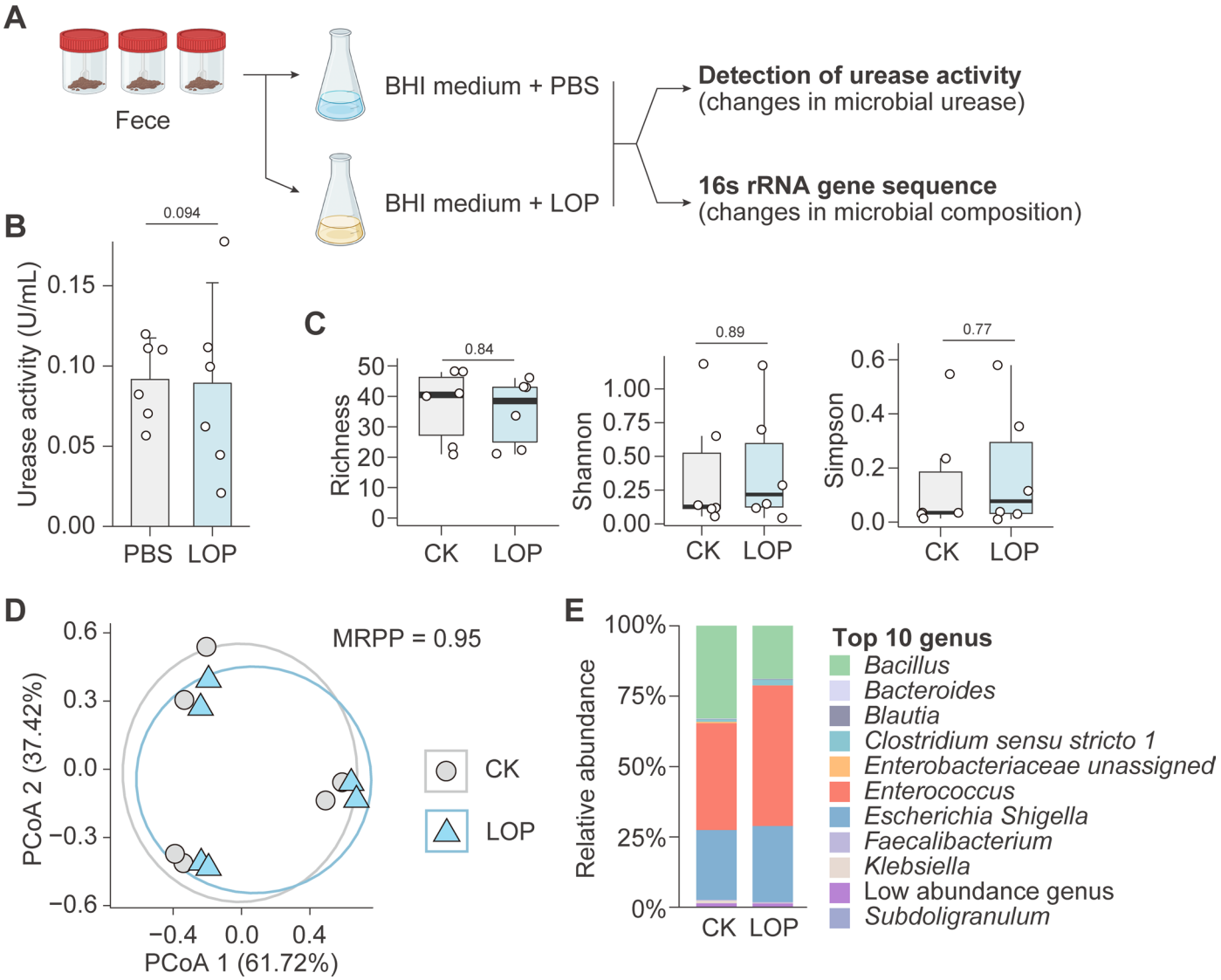
Extended Data Fig. 1 | Alternations of microbial ACh metabolic pathway after intestinal dysmotility in both mice and human cohort. (**A**) Summary of genes involved in synthesis and degradation of ACh and choline, based on the KEGG database. Genes associated with the ACh metabolic pathway were identified from gut metagenomes of LOP mice (**B**) and examined their abundance alterations following LOP treatment (n = 5/group) (**C**). Genes associated with the ACh metabolic pathway were identified from gut metagenomes of public human cohort with intestinal dysmotility (**D**) and examined their abundance alterations (n = 95 in Health and n = 80 in Constipation) (**E**). Boxplots in C (center line or point, median; box limits, 25th and 75th percentile; whiskers, Tukey's method (1.5× interquartile range)). Statistical significance was determined using two-tailed Student's t-test. Illustrations in B and D were created using BioRender (https://biorender.com).

https://doi.org/10.1038/s41564-026-02269-8



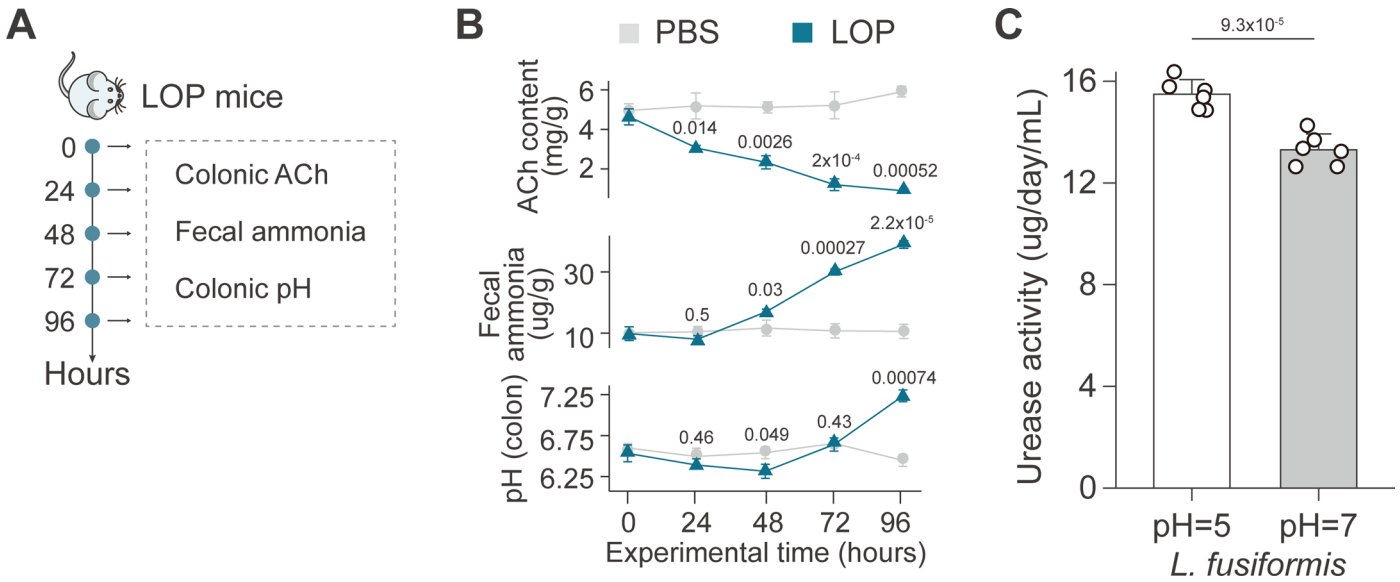
Extended Data Fig. 2 | Bioinformatics analysis of gut microbiome from LOP-mice and public human cohort with intestinal dysmotility. (**A**) Differential analysis on functional genes after LOP treatment in mice. Statistical comparisons were conducted using unpaired two-tailed Student's t-test with Benjamini/Hochberg correction. (**B**) Workflow of analysis of public human cohort with dysmotility and database. (**C**) Changes of urease between two public human cohorts (n = 129 in Health and 102 in Constipation for dataset 1, n = 60 in Health and 58 in Constipation for dataset 2). Changes of taxonomic composition of gut microbiota based on the 16S rRNA gene sequencing, included Gini-Simpson (n = 5/group) (**D**) and NMDS analysis (**E**) of gut microbiota based on the Bray-Curtis distance. Boxplots in C (center line or point, median; box limits, 25th and 75th percentile; whiskers, Tukey's method (1.5× interquartile range); points, outliers). Boxplots in D (center line or point, median; box limits, 25th and 75th percentile; whiskers, Tukey's method (1.5× interquartile range); diamond, outliers). Statistical significance was determined using two-tailed Student's t-test.

https://doi.org/10.1038/s41564-026-02269-8



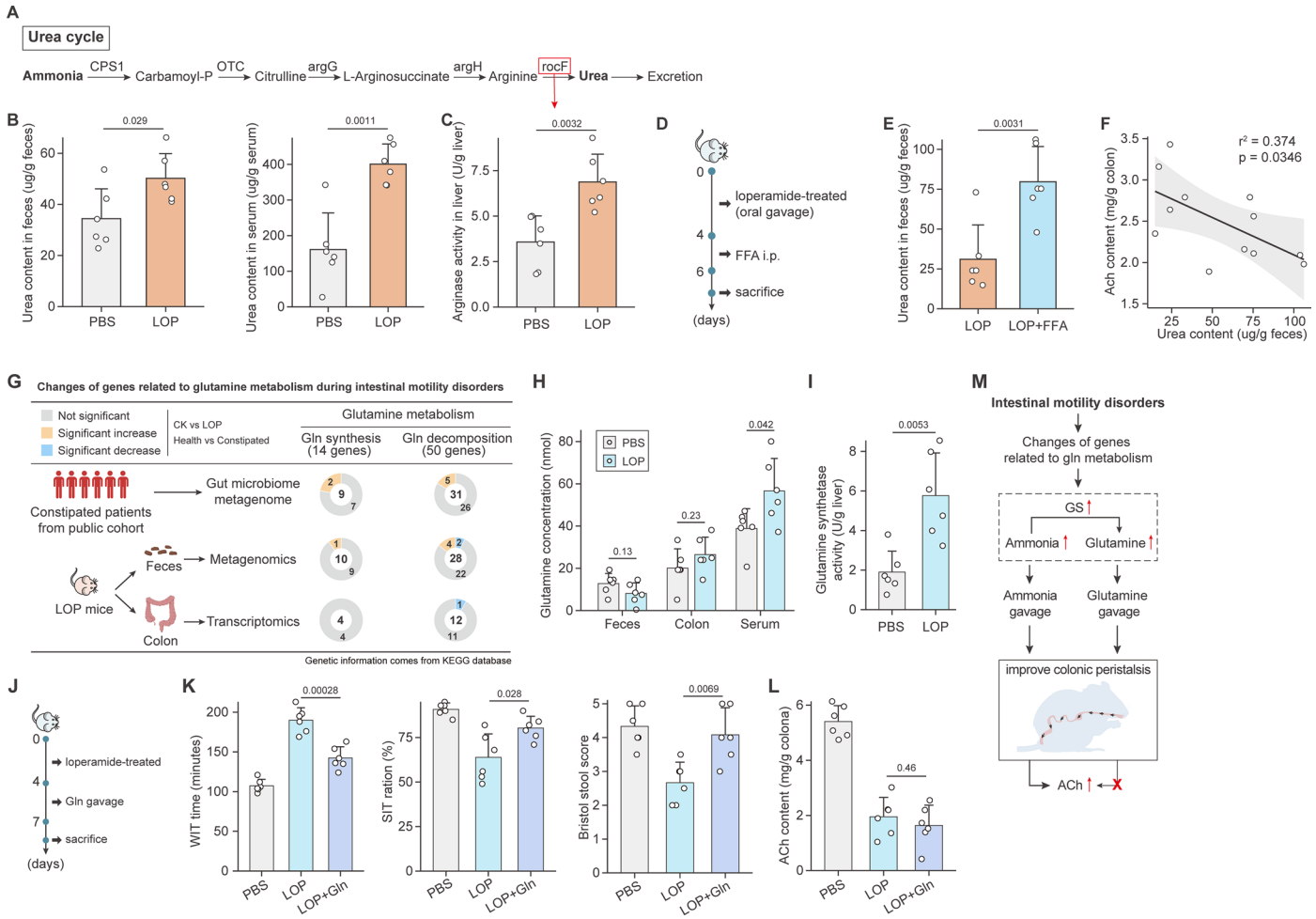
Extended Data Fig. 3 | Healthy human fecal samples were cultured in vitro with LOP to assess its direct effects on the gut microbiota. (**A**) Workflow of the co-culture of healthy human feces with LOP. (**B**) Change of urease activity after LOP intervention (n = 6/group). Changes of taxonomic composition of microbiota after co-culture based on the 16S rRNA gene sequencing, included alpha diversity (n = 6/group) (**C**), PCoA analysis (**D**) of gut microbiota based on the Bray-Curtis distance and taxonomic composition (**E**). All data represent mean ± s.d. of at least 3 biologically independent experiments, except for boxplots in C (center line or point, median; box limits, 25th and 75th percentile; whiskers, Tukey's method (1.5× interquartile range)). Statistical significance was determined using two-tailed Student's t-test. Illustrations in A was created using BioRender (https://biorender.com).

https://doi.org/10.1038/s41564-026-02269-8



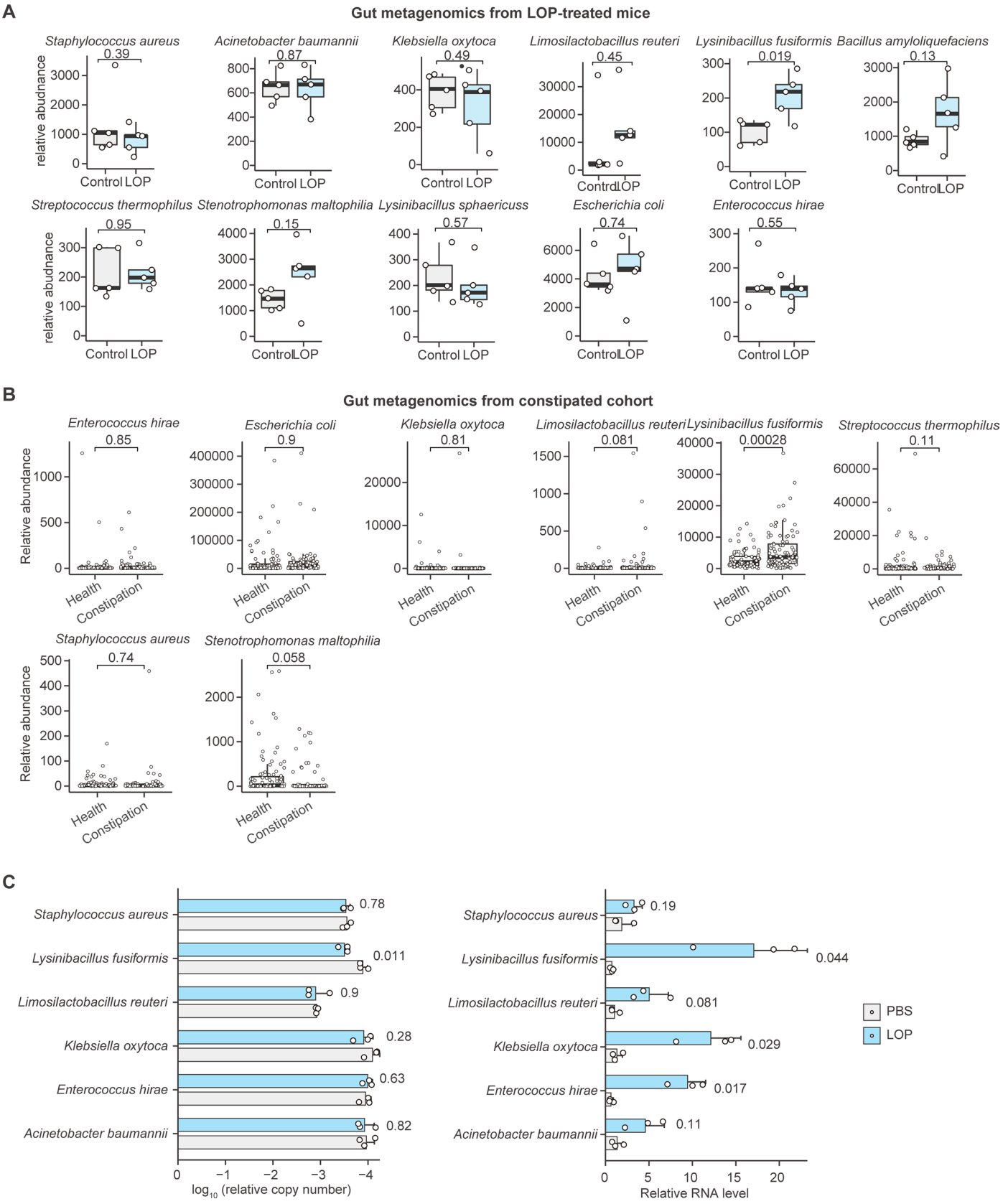
Extended Data Fig. 4 | Relationship between colonic ACh, luminal pH and fecal ammonia during intestinal dysmotility. (**A**) Longitudinal sampling schematic and temporal dynamics of colonic ACh, luminal pH and fecal ammonia levels. (**B**) Alterations in colonic ACh, luminal pH and fecal ammonia levels during intestinal dysmotility (n = 5/group). (**C**) Changes of urease activity of L. fusiformis cultured in different pH medium (n = 6/group). All data represent mean ± s.d. of at least 3 biologically independent experiments. Statistical significance was determined using two-tailed Student's t-test. Illustrations in A was created using BioRender (https://biorender.com).

https://doi.org/10.1038/s41564-026-02269-8



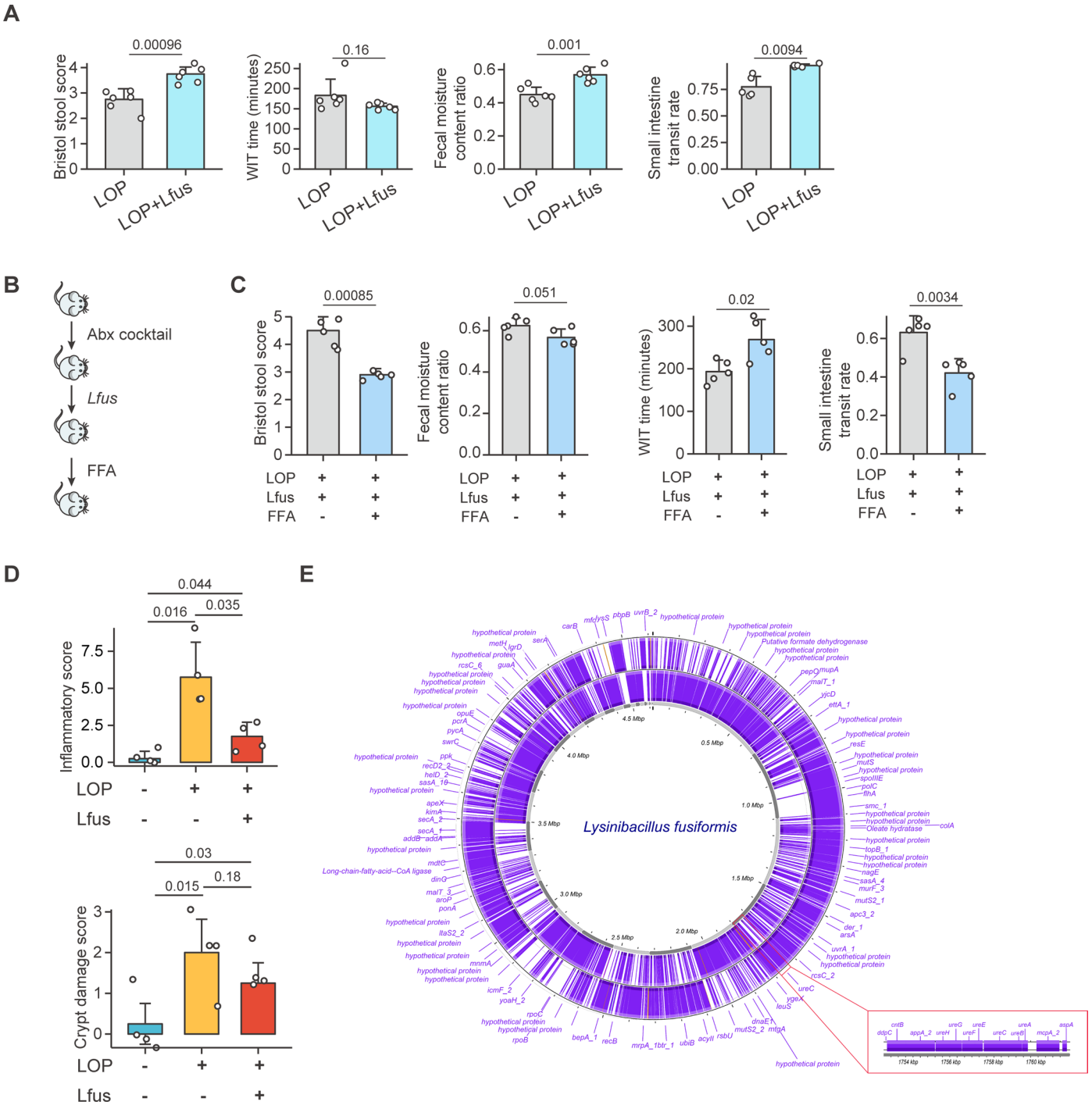
Extended Data Fig. 5 | The role of urea cycle and glutamine metabolism in intestinal dysmotility. (**A**) Metabolites and Genes Involved in the Urea Cycle. (**B**) Changes of urea levels in feces and serum after LOP treatment (n = 6/group). (**C**) Change of arginase activity in liver in LOP mice (n = 6/group). (**D**) Workflow of FFA treatment on LOP mice. (**E**) Alternation of urea levels in feces after FFA-treated on LOP-mice (n = 6/group). (**F**) Regression analysis between colonic ACh levels and fecal urea levels. Solid lines represent ordinary least-squares linear regressions, and the error bands indicate the 95% confidence intervals. (**G**) Summary of genes involved in synthesis and degradation of Gln based on the KEGG database, and genes associated with the Gln metabolic pathway were identified from gut metagenomes, colonic RNA-seq of LOP mice and gut metagenomes of public human cohort with intestinal dysmotility. (**H**) Alternations of Gln levels in feces, colon and serum after LOP treatment (n = 6/group). (**I**) Changes of Gln synthetase activity in liver (n = 6/group). (**J**) Workflow of Gln treatment on LOP-mice. (**K**) Assessment of intestinal motility in Gln-treated LOP-mice (n = 6/group). (**L**) Alternations of colonic ACh levels after Gln intervention (n = 6/group). (**M**) The role of Gln metabolism in the ammonia-ACh axis-mediated intestinal motility mechanism. All data represent mean ± s.d. of at least 3 biologically independent experiments. Statistical significance was determined using two-tailed Student's t-test. Illustrations in D and G were created using BioRender (https://biorender.com).

https://doi.org/10.1038/s41564-026-02269-8



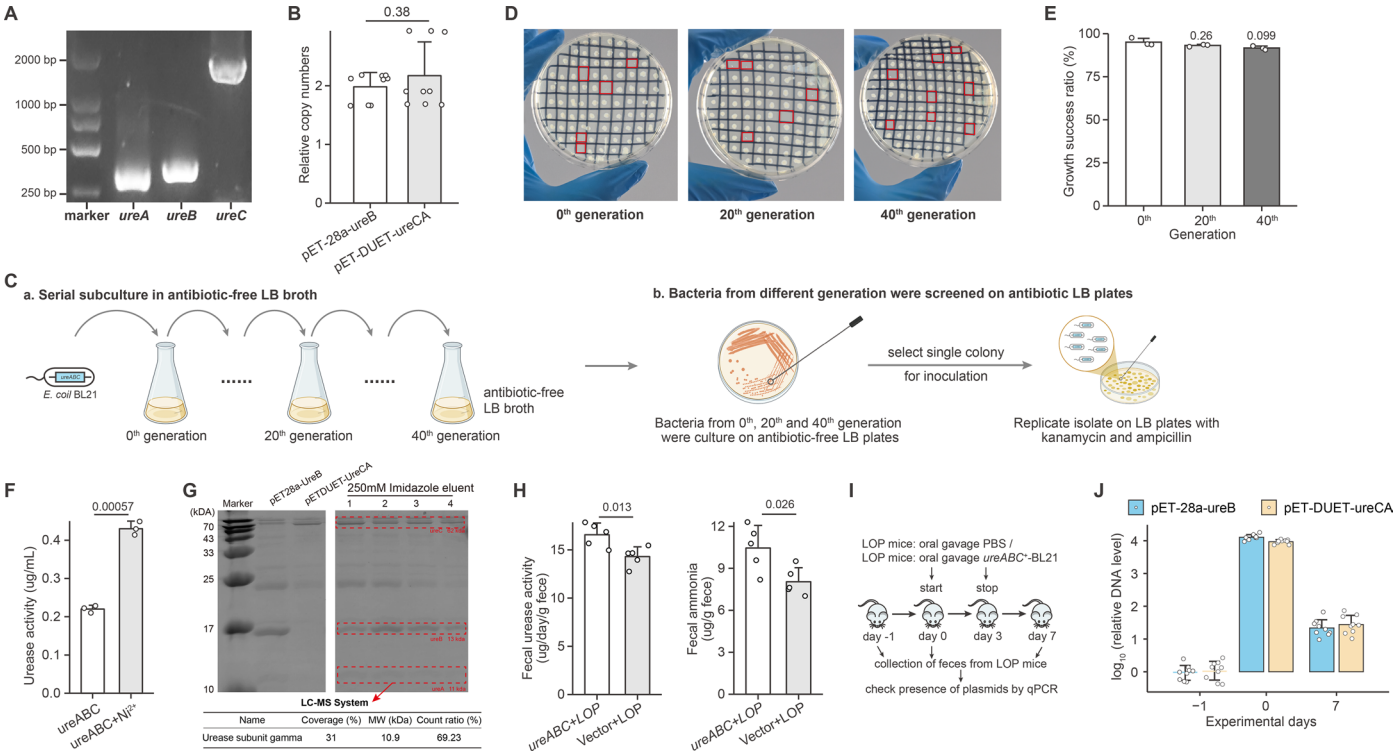
Extended Data Fig. 6 | Alternations of urease-positive isolates in intestinal dysmotility. (**A**) Changes of abundance of urease-positive isolates in LOP-mice's gut metagenomes (n = 5/group). (**B**) Changes of abundance of urease-positive isolates in public human cohort's gut metagenomes (n = 95 in Health and n = 58 in Constipation). (**C**) Changes of relative copy numbers of six representative isolates and relative RNA levels of urease coded gene (n = 3/group). All data represent mean ± s.d. of at least 3 biologically independent experiments, except for boxplots in A and B (center line or point, median; box limits, 25th and 75th percentile; whiskers, Tukey's method (1.5× interquartile range)). Statistical analysis assessed by two-tailed Student's t-test.

https://doi.org/10.1038/s41564-026-02269-8



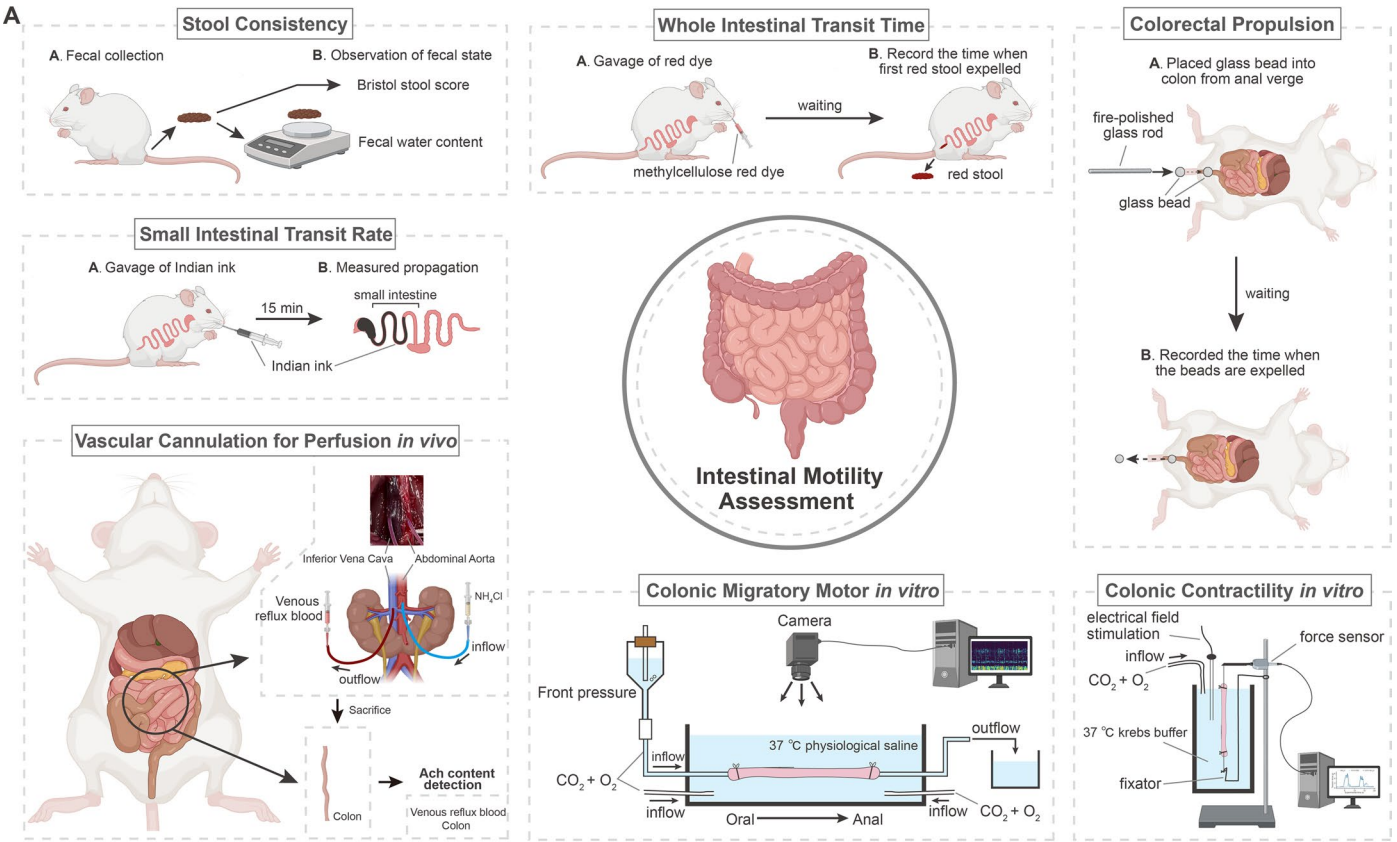
Extended Data Fig. 7 | The intervention of L. fusiformis on LOP-mice in different conditions. (**A**) Assessment of intestinal motility after treating with L. fusiformis on LOP mice (n = 6/group). (**B**) and (**C**) Assessment of intestinal motility after treating with FFA on L. fusiformis-treated LOP mice (n = 5/group). (**D**) Inflammatory score and crypt damage score of colon tissue (n = 4/group). (**E**) Analysis of whole-genome sequencing on L. fusiformis and sequence information of urease-coding genes. All data represent mean ± s.d. of at least 3 biologically independent experiments. Statistical analysis assessed by two-tailed Student's t-test.

https://doi.org/10.1038/s41564-026-02269-8



Extended Data Fig. 8 | Protein expression and plasmid stability in recombinant BL21. (**A**) Agarose gel electrophoresis of ureA, ureB, and ureC genes from recombinant BL21 single clones (n = 9/group). (**B**) Relative copy number of two plasmids in recombinant BL21. (**C**) Workflow of serial passaging under antibiotic-free conditions followed by selection on double-antibiotic plates for recombinant BL21. (**D**) Growth of recombinant BL21 and its success ratio (**E**) on double-antibiotic plates following serial passaging (n = 3/group). (**F**) Change of urease activity with or without Ni2+ (n = 3/group). (**G**) Tris-Tricine-SDS-PAGE gel indicating specific expression of the ureABC and LC-MS sequencing of ureA. (**H**) Change of urease activity and fecal ammonia in feces after intervention of recombinant BL21 (n = 5/group). (**I**) Workflow of collection of feces from mice treated with recombinant BL21. (**J**) Fecal copy numbers of the two plasmids during recombinant BL21 intervention in mice (n = 9/group). All data represent mean ± s.d. of at least 3 biologically independent experiments. Statistical significance was determined using two-tailed Student's t-test. Illustrations in C and I were created using BioRender (https://biorender.com).

https://doi.org/10.1038/s41564-026-02269-8



Extended Data Fig. 9 | Integrated methods for evaluating intestinal motility. (**A**) Methods for assessing intestinal motility including in vivo and in vitro. (**B**) Spatiotemporal maps show CMMCs (white arrows) in isolated colons of LOP and LOP+NH4Cl mice. (**C**) Change of fecal ammonia level in different intervention mice (n = 6/group). (**D**) The formula for converting fecal ammonia at physiological concentrations to millimolar (mM) units, assuming a fecal density of 1 g/mL. All data represent mean ± s.d. of at least 3 biologically independent experiments. Statistical significance was determined using two-tailed Student's t-test. Illustrations in A was created using BioRender (https://biorender.com).